The Astronomical Journal, 154:264 (19pp), 2017 December https://doi.org/10.3847/1538-3881/aa984b

Validation of Small *Kepler* Transiting Planet Candidates in or near the Habitable Zone

Guillermo Torres[1], Stephen R. Kane[2], Jason F. Rowe[3], Natalie M. Batalha[4], Christopher E. Henze[4], David R. Ciardi[5], Thomas Barclay[6], William J. Borucki[4], Lars A. Buchhave[7], Justin R. Crepp[8], Mark E. Everett[9], Elliott P. Horch[10,11,14], Andrew W. Howard[12], Steve B. Howell[4], Howard T. Isaacson[13], Jon M. Jenkins[4], David W. Latham[1], Erik A. Petigura[12,15], and Elisa V. Quintana[6]

[1] Harvard-Smithsonian Center for Astrophysics, 60 Garden Street, Cambridge, MA 02138, USA; gtorres@cfa.harvard.edu
[2] Department of Earth Sciences, University of California, Riverside, CA 92521, USA
[3] Department of Physics and Astronomy, Bishop's University, 2600 College Street, Sherbrooke, QC, J1M 1Z7, Canada
[4] NASA Ames Research Center, Moffett Boulevard, Moffett Field, CA 94035, USA
[5] NASA Exoplanet Science Institute/Caltech, Pasadena, CA 91125, USA
[6] NASA Goddard Space Flight Center, Greenbelt, MD 20771, USA
[7] Centre for Star and Planet Formation, Natural History Museum of Denmark & Niels Bohr Institute, University of Copenhagen, DK-1350 Copenhagen K, Denmark
[8] Department of Physics, University of Notre Dame, Notre Dame, IN 46556, USA
[9] National Optical Astronomy Observatory, Tucson, AZ 85719, USA
[10] Department of Physics, Southern Connecticut State University, New Haven, CT 06515, USA
[11] Lowell Observatory, 1400 W Mars Hill Road, Flagstaff, AZ 86001, USA
[12] California Institute of Technology, 1200 E California Boulevard, Pasadena, CA 91125, USA
[13] Astronomy Department, University of California, Berkeley, CA 94720, USA
Received 2017 August 11; revised 2017 November 1; accepted 2017 November 1; published 2017 December 1

Abstract

A main goal of NASA's *Kepler* Mission is to establish the frequency of potentially habitable Earth-size planets ($\eta_\oplus$). Relatively few such candidates identified by the mission can be confirmed to be rocky via dynamical measurement of their mass. Here we report an effort to validate 18 of them statistically using the BLENDER technique, by showing that the likelihood they are true planets is far greater than that of a false positive. Our analysis incorporates follow-up observations including high-resolution optical and near-infrared spectroscopy, high-resolution imaging, and information from the analysis of the flux centroids of the *Kepler* observations themselves. Although many of these candidates have been previously validated by others, the confidence levels reported typically ignore the possibility that the planet may transit a star different from the target along the same line of sight. If that were the case, a planet that appears small enough to be rocky may actually be considerably larger and therefore less interesting from the point of view of habitability. We take this into consideration here and are able to validate 15 of our candidates at a 99.73% (3σ) significance level or higher, and the other three at a slightly lower confidence. We characterize the GKM host stars using available ground-based observations and provide updated parameters for the planets, with sizes between 0.8 and 2.9 $R_\oplus$. Seven of them (KOI-0438.02, 0463.01, 2418.01, 2626.01, 3282.01, 4036.01, and 5856.01) have a better than 50% chance of being smaller than 2 $R_\oplus$ and being in the habitable zone of their host stars.

Key words: methods: statistical – planetary systems – stars: individual (KOI-0172.02 = Kepler-69c ...) – techniques: photometric

1. Introduction

The occurrence rate of terrestrial-size planets within the habitable zone (HZ) of their host stars, referred to as "eta Earth," or $\eta_\oplus$, is one of the fundamental quantities that the exoplanet community is focusing their efforts on. The vast numbers of transiting planet candidates from the *Kepler* Mission (Borucki 2016) are the primary source for these calculations, and there have been many efforts to estimate the value of $\eta_\oplus$ from those data (see the recent examples of Dressing & Charbonneau 2013; Kopparapu 2013; Burke et al. 2015; Dressing & Charbonneau 2015; Mulders et al. 2015, and references therein). A key aspect of determining the reliability of these estimates is the confirmation of *Kepler* candidates (*Kepler* Objects of Interest, or KOIs), particularly for earlier-type stars for which the orbital periods for the habitable zone become increasingly longer and the data more prone to false positives (Burke et al. 2015; Coughlin et al. 2016).

Many of the *Kepler* stars that appear to host small planets in the HZ are faint or have other properties such as significant rotation or chromospheric activity that make it very difficult to obtain the high-precision radial-velocity measurements needed for a dynamical confirmation of the planetary nature of the candidate. KOIs with long orbital periods (P) are even more challenging as the radial-velocity amplitudes fall off as $P^{-1/3}$, resulting in Doppler signals that are often of the order of 1 m s^{-1} or less, which is at the limit of the detection capabilities of present instrumentation and techniques.

Kane et al. (2016) recently published a catalog of transiting HZ candidates from *Kepler* based on the best available set of planetary and stellar parameters available to them. Many of these candidates are nominally smaller than 2 $R_\oplus$ and have relatively long orbital periods up to several hundred days. These KOIs are therefore of great interest in connection with efforts to establish $\eta_\oplus$, and yet most of them have remained unconfirmed for one or more of the reasons mentioned above.

An alternative to dynamical confirmation is statistical validation, in which the goal is to show that the likelihood of a false positive is much smaller than that of a true planet.

[14] Adjunct Astronomer.
[15] NASA Hubble Fellow.

A number of the candidates presented by Kane et al. (2016) have been validated by others and have subsequently received official *Kepler* planet designations. However, in most cases, those validation studies have only been concerned with demonstrating the presence of a planet associated with the target but not necessarily orbiting it. In particular, in reporting a confidence level for the validation, they have usually not accounted for the possibility that the planet may instead transit an unresolved star near the target, either physically bound to it, or a chance alignment (Lissauer et al. 2014; Morton et al. 2016). Such situations can in fact be more common than the types of false positives normally considered in these validation studies, by one to three orders of magnitude (see, e.g., Fressin et al. 2013; Torres et al. 2015). If the planet orbits a different star, the transit signal observed would not reflect the true size of the planet. Instead, the true size could be considerably larger (Ciardi et al. 2015; Furlan et al. 2017), possibly implying an icy or gaseous composition rather than a rocky one. This would make the planet less interesting from the standpoint of habitability and $\eta_{\oplus}$.

The motivation for the present work is thus to examine each of the most promising *Kepler* HZ candidates more closely and revisit the validations with attention to this issue, making use of follow-up observations and other constraints not previously available. We use these observations to also provide updated parameters for the validated planets.

This paper is organized as follows. The target selection for this work is explained in Section 2, followed by a description of the *Kepler* photometry we use. Section 4 presents the follow-up observations for the targets, which includes high-resolution imaging, an analysis of the motion of the flux centroids, and high-resolution spectroscopy. Then, in Section 5, we describe our analysis of the spectroscopic material to determine the stellar properties of the host stars (temperatures, metallicities, masses, radii, mean densities, ages, etc.). The statistical validation procedure and results are presented in Section 6, after which we report our light-curve fits that yield the planetary parameters (Section 7). The habitability of the planets is discussed in Section 8, and the last section features our concluding remarks.

2. Target Selection

The source of our target list is an early version of the catalog of small HZ candidates published by Kane et al. (2016), which in turn is the product of the efforts by the *Kepler* HZ Working Group to evaluate the full set of candidates observed during the mission's quarters 1 through 17 (Q1–Q17). This catalog describes the various definitions used by different authors for the HZ and chose to consider both an "optimistic" (larger) HZ and a "conservative" (smaller) HZ, based on the assumptions of Kopparapu et al. (2014) informed by estimates of how long Venus and Mars may have been able to retain liquid water on their surfaces. For reference, the inner and outer boundaries adopted for the optimistic HZ correspond to approximately 0.75 and 1.8 au for a star like the Sun, and those of the conservative HZ are located at about 0.99 and 1.7 au, although these limits vary depending on the exact temperature of the star because of changes in the albedo of an Earth-like planet under the different wavelengths of stellar irradiation. The compilation of Kane et al. (2016) also separated the candidates according to their size (planetary radius R_p), defining four categories as follows, with some being subsets of others:

1. Candidates in the conservative HZ with $R_p \leqslant 2\,R_{\oplus}$;
2. Candidates in the optimistic HZ with $R_p \leqslant 2\,R_{\oplus}$;
3. Candidates in the conservative HZ with any radius;
4. Candidates in the optimistic HZ with any radius.

The present work began during the early stages of preparation of the catalog of Kane et al. (2016) with the selection of 19 candidates for validation from Categories 1 and 2, which were ranked to be of high interest based on their small size and likelihood of being in the HZ. However, due in part to subsequent improvements in the stellar parameters (particularly the stellar radii and temperatures) that led to revised planetary parameters, the KOIs considered for inclusion in the Kane et al. (2016) catalog evolved with time until its publication, and as a result not all of the targets we initially selected for validation ended up in the final version of the catalog. On the other hand, out of concern that some of the signals might be spurious, we had originally chosen to exclude candidates in the catalog with low or marginal signal-to-noise ratios (S/Ns) as represented by the Multiple Event Statistic (MES) listed on NASA's Exoplanet Archive.[16] The MES measures the significance of the observed transits in the detrended, whitened light curve (Jenkins et al. 2002). We rejected KOIs with MES values lower than about 10, based on the estimates from the *Kepler* data release current at the time (Q1–Q17 Data Release 24, or DR24; Coughlin et al. 2016). The most recent and final data release (DR25; Thompson et al. 2017) did not alter that selection except in the case of KOI-7235.01, which was accepted by Kane et al. (2016) but is now considered to be a false alarm. We therefore dropped this candidate from the target list and retained the other 18. Six of these are in Category 1, three additional ones are in Category 2, two more are in Category 3, and one is in Category 4. The other six of our original targets are not listed in any of the categories of the catalog of Kane et al. (2016).

Table 1 presents the set of targets we kept for this study and includes the *Kepler* planet designation when the candidate was statistically validated previously or as a result of this work, along with the MES and transit depth as listed on the Exoplanet Archive, and other ancillary information.

3. Photometry

Kepler photometry for all targets was retrieved from the Mikulski Archive for Space Telescopes (MAST)[17]. The observations used here are those labeled in the FITS files as PDC_FLUX, based on Data Release 25. Our targets have a mix of Long Cadence (LC) observations with ∼30 minute samples and Short Cadence (SC) observations with ∼1 minute sampling, and SC observations took precedence when both LC and SC were available for any observation window.

The PDC photometry adopted for our analysis includes corrections for instrumental trends as well as estimates of dilution due to other stars that contaminate the photometric aperture (Stumpe et al. 2014). Additionally, we accounted for further dilution from close companions to our targets identified via high-resolution imaging (see Section 4), both in our false-positive assessments (Section 6) and in our transit light-curve modeling (Section 7). We did not rescale the PDC photometry based on additional information regarding aperture dilution.

[16] http://exoplanetarchive.ipac.caltech.edu/
[17] https://archive.stsci.edu/index.html

Table 1
Sample of KOIs in This Study

Candidate	Name	KID	*Kp* (mag)	*b* (degrees)	Period (days)	MES	Depth (ppm)
KOI-0172.02	Kepler-69 c (1)	8692861	13.749	+11.99	242.47	18.0	340
KOI-0438.02	Kepler-155 c (2)	12302530	14.258	+17.45	52.66	30.6	1078
KOI-0463.01	Kepler-560 b (3)	8845205	14.708	+7.76	18.48	78.0	2605
KOI-0812.03	Kepler-235 e (2)	4139816	15.954	+14.48	46.18	18.0	1395
KOI-0854.01	Kepler-705 b (3)	6435936	15.849	+13.13	56.06	19.3	1626
KOI-2418.01	Kepler-1229b (3)	10027247	15.474	+10.38	86.83	11.7	751
KOI-2626.01	Kepler-1652 b	11768142	15.931	+13.57	38.10	14.6	913
KOI-2650.01	Kepler-395 c (2)	8890150	15.987	+11.96	34.99	10.1	498
KOI-3010.01	Kepler-1410b (3)	3642335	15.757	+11.13	60.87	12.7	714
KOI-3282.01	Kepler-1455b (3)	12066569	15.855	+13.99	49.28	14.7	1133
KOI-3497.01	Kepler-1512b (3)	8424002	13.393	+14.39	20.36	19.6	346
KOI-4036.01	Kepler-1544b (3)	11415243	14.061	+11.56	168.81	14.8	614
KOI-4054.01	⋯	6428794	14.566	+15.14	169.13	16.7	641
KOI-4356.01	Kepler-1593b (3)	8459663	15.873	+7.30	174.51	11.0	1530
KOI-4450.01	Kepler-1606b (3)	7429240	15.139	+15.75	196.44	11.1	632
KOI-4550.01	Kepler-1653 b	5977470	15.429	+8.25	140.25	9.6	568
KOI-5236.01	⋯	6067545	13.093	+7.01	550.86	12.1	346
KOI-5856.01	Kepler-1638b (3)	11037818	14.759	+12.29	259.34	10.9	350

Note. Columns after the first indicate the *Kepler* planet designation and source, *Kepler* identification number, brightness in the *Kepler* passband, Galactic latitude, orbital period, multiple event statistic, and transit depth in parts per million relative to the out-of-transit stellar flux. For consistency in this paper, we will refer to all objects by their original KOI names throughout. The sources of the *Kepler* planet designations are the following: (1) Barclay et al. (2013), (2) Rowe et al. (2014), (3) Morton et al. (2016), (4) New designation based on this work.

To minimize the impact of stellar variability on our transit models described later, we applied a polynomial filter to remove variability on timescales longer than 5 days, as described in Section 4 of Rowe et al. (2014). A bandpass of five days was chosen to be significantly longer than the longest observed transit duration in our sample, which is 15.9 hr for KOI-5856.01 (Kepler-1638b).

4. Follow-up Observations and Centroid Motion Analysis

4.1. High-resolution Imaging

Each of our targets has been subjected to high spatial resolution imaging to detect close stellar companions that could be the source of the transit signals we observe, if those companions are eclipsed by another body. Even if they are not eclipsing and the planet orbits the KOI, these companion stars can still attenuate the transit signal and make the planet appear smaller than it really is.

Furlan et al. (2017) have recently published a compilation of all the information from the imaging observations performed on more than 1900 stars observed by *Kepler*. For our sample, we have images gathered mainly with the following instruments and telescopes: adaptive optics observations on the Keck II 10 m telescope with the NIRC2 instrument (Wizinowich et al. 2004) in the *J* band (1.246 μm) or K' band centered on Brγ (2.18 μm); adaptive optics on the 5 m Palomar telescope with the PHARO instrument (Hayward et al. 2001) in *H* (1.635 μm) or K_s (2.145 μm); adaptive optics with the Robo-AO system on the Palomar 1.5 m telescope (Baranec et al. 2016) using a long-pass filter (LP600) starting at 600 nm, making it similar to the *Kepler* passband; speckle interferometry on the Gemini-N 8 m telescope and on the DCT 4 m telescope with the DSSI instrument (Horch et al. 2009; Horch et al. 2010) obtained at wavelengths of 562 nm (Gemini-N only), 692 nm, or 880 nm; and in two cases, we used the imaging with the F555W filter of WFC3 on the *HST* as reported by Gilliland et al. (2015).

A total of eight of our KOIs have close companions reported by Furlan et al. (2017) within 4″, occasionally more than one per target. They are listed in Table 2 along with the relative position and brightness difference compared to the primary star. Some of those companions are close enough that they cannot be ruled out as potential sources of the signal by the centroid motion analysis described in the next section and are flagged in the table. We discuss them further in Section 6.

For each star in our sample, we also estimated our ability to detect companions at close separations. This information is critical to our analysis described later to validate the candidates. When not already available on the Exoplanet Follow-up Observing Program (ExoFOP) Web page,[18] we used numerical simulations to produce sensitivity curves of detectable companion brightness as a function of angular separation as described by Torres et al. (2015) and Furlan et al. (2017), or adopted published sensitivity curves in the case of the Robo-AO and *HST* observations. In two cases, we adopted published sensitivity curves for the Keck observations by Kraus et al. (2016). Figure 1 shows the curves that provide the strongest constraints on unseen companions for each KOI. We note that for several of our targets, we used sensitivity curves from several instruments or at several wavelengths at the same time, to maximize our ability to rule out blends.

4.2. Centroid Motion

The positions of the flux centroids of our stars offer an additional and powerful discriminant against false positives and can provide evidence that the source of the signal is not on the target if the image centroid moves significantly in and out of transit. The Data Validation Reports from the *Kepler* Science

[18] https://exofop.ipac.caltech.edu/cfop.php

Table 2
Close Companions from High-resolution Imaging

Star	ρ ($''$)[a]	P.A. (degrees)	Brightness Difference (mag) and Passband
KOI-0438	3.290 ± 0.059	182.0 ± 1.2	3.11 ± 0.04 (LP600), 2.245 ± 0.010 (*J*), 2.160 ± 0.010 (*K*)
KOI-0854	0.016 ± 0.050*	209.4 ± 1.0	0.299 ± 0.231 (*K*)
KOI-0854	0.154 ± 0.050*	181.6 ± 1.0	3.589 ± 0.076 (*K*)
KOI-2418	0.108 ± 0.050*	3.2 ± 1.6	3.22 ± 0.15 (692 nm), 2.94 ± 0.15 (880 nm), 2.509 ± 0.062 (*K*)
KOI-2418	2.387 ± 0.050	104.4 ± 1.0	7.793 ± 0.086 (*K*)
KOI-2418	3.918 ± 0.066	329.2 ± 1.5	5.45 ± 0.16 (*J*), 6.845 ± 0.035 (*K*)
KOI-2626	0.164 ± 0.050*	183.4 ± 3.4	1.646 ± 0.094 (F555W), 1.302 ± 0.094 (F775W), 1.95 ± 0.15 (562 nm), 2.22 ± 0.15 (692 nm), 1.28 ± 0.15 (880 nm) 0.91 ± 0.19 (*K*)
KOI-2626	0.206 ± 0.050*	212.7 ± 1.4	0.763 ± 0.071 (F555W), 0.509 ± 0.071 (F775W), 1.91 ± 0.15 (562 nm), 1.63 ± 0.15 (692 nm), 0.88 ± 0.15 (880 nm) 0.464 ± 0.079 (*K*)
KOI-2650	3.121 ± 0.050	124.8 ± 1.0	8.200 ± 0.059 (F555W), 7.577 ± 0.031 (F775W), 7.252 ± 0.079 (*K*)
KOI-3010	0.334 ± 0.050*	304.5 ± 1.1	0.595 ± 0.050 (F555W), 0.294 ± 0.050 (F775W), 0.74 ± 0.15 (692 nm), 0.01 ± 0.15 (880 nm), 0.245 ± 0.052 (*K*)
KOI-3497	0.795 ± 0.064*	174.1 ± 1.8	1.23 ± 0.12 (LP600), 1.31 ± 0.47 (*K*)
KOI-4550	1.045 ± 0.069*	143.7 ± 1.3	0.040 ± 0.020 (LP600), 0.75 ± 0.15 (692 nm), 1.11 ± 0.15 (880 nm), 0.578 ± 0.010 (*J*)
KOI-5236	1.943 ± 0.050*	283.4 ± 1.0	6.398 ± 0.028 (*K*)

Note.
[a] Companions flagged with an asterisk are inside the limits of the 3σ exclusion region from the centroid motion analysis (Table 3) and thus cannot be rejected as potential false-positive sources in that way.

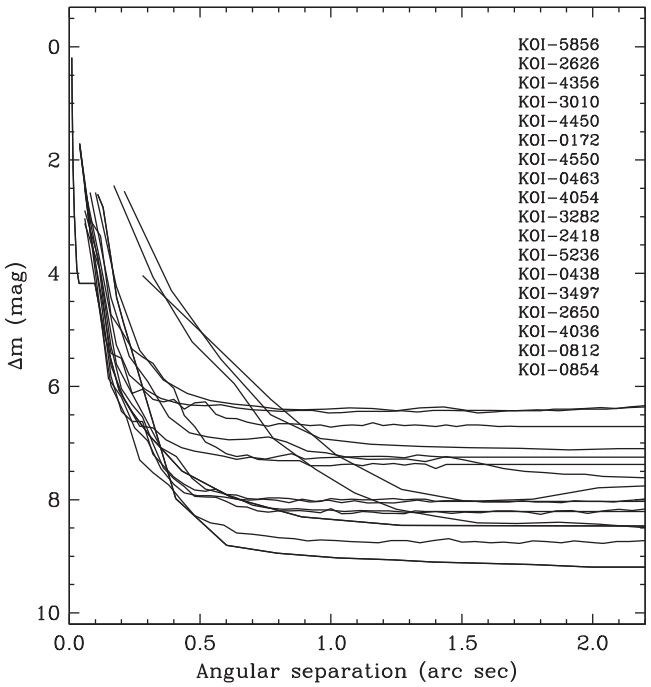

Figure 1. Sensitivity curves for each of our targets from the high-resolution imaging observations that provide the strongest constraints on unseen companions. Curves correspond to the KOIs as listed, top to bottom, at a reference separation of 2″. The measurements shown are based on Keck AO images in the (2.124 μm) K' band, with the exception of KOI-0812 and KOI-0854, for which we show curves for the F555W passband of *HST* as measured by Gilliland et al. (2015).

Operations Center pipeline, also available on the NASA Exoplanet Archive, list a measure of this offset for each quarter computed by subtracting the best-fit pixel response function centroid out of transit from the difference image centroid (see Bryson et al. 2013), as well as a multiquarter average and its uncertainty. If the source of a transit is located less than 3σ from the host star, it is considered to be statistically indistinguishable from the host star. This 3σ exclusion radius is mainly a function of the S/N of the transit signal.

Table 3
Centroid Results for the Candidates

Candidate	Offset from Star ($''$)	Offset from Star (σ)	3σ Exclusion Radius ($''$)
KOI-0172.02	1.46 ± 0.59	2.47	1.77
KOI-0438.02	0.26 ± 0.18	1.48	0.54
KOI-0463.01	0.03 ± 0.08	0.35	0.24
KOI-0812.03	0.08 ± 0.20	0.37	0.64
KOI-0854.01	0.35 ± 0.38[a]	0.93	1.13[a]
KOI-2418.01	0.27 ± 0.28	0.97	0.84
KOI-2626.01	0.62 ± 0.86[a]	0.72	2.57[a]
KOI-2650.01	0.53 ± 0.57	0.94	1.70
KOI-3010.01	0.62 ± 1.58[a]	0.39	4.73[a]
KOI-3282.01	0.14 ± 0.33	0.42	0.99
KOI-3497.01	0.14 ± 0.45[a]	0.32	1.34[a]
KOI-4036.01	0.62 ± 0.34	1.80	1.03
KOI-4054.01	0.32 ± 0.32	1.01	0.95
KOI-4356.01	0.99 ± 0.58	1.71	1.73
KOI-4450.01	0.57 ± 0.42	1.35	1.28
KOI-4550.01	1.17 ± 1.26[a]	0.93	3.79[a]
KOI-5236.01	1.07 ± 0.99	1.09	2.96
KOI-5856.01	0.59 ± 0.32	1.84	0.97

Note.
[a] Offset uncertainties and corresponding 3σ exclusion regions conservatively doubled in size to account for possible biases due to the presence of close and relatively bright companions.

In Table 3, we list the in-and-out-of-transit offsets and their uncertainties as reported for each of our targets in the NASA Exoplanet Archive, in arcseconds and also in units of the uncertainties (σ). The last column gives the corresponding 3σ exclusion radii. In all cases, the KOIs have offsets that are less than three times their uncertainties, thus suggesting the targets are the source of the signals. These exclusion regions are small enough that they rule out some of the wider companions reported in the previous section, but not all. We note, on the

Table 4
Optical Spectra for Our Targets

	Keck/HIRES		TRES		McDonald		KPNO		
Star	BJD	S/N	BJD	S/N	BJD	S/N	BJD	S/N	RV (km s^{-1})
KOI-0172	2455735.8686	58.7	2456462.8167	26.9	⋯	⋯	⋯	⋯	−41.2
KOI-0438	2456147.9907	27.3	⋯	⋯	⋯	⋯	⋯	⋯	−11.6
KOI-0463	2456028.1245	18.5	⋯	⋯	⋯	⋯	⋯	⋯	−96.8
KOI-0812	2456166.0273	13.4	⋯	⋯	⋯	⋯	⋯	⋯	−30.6
KOI-0854	2456172.8635	16.8	⋯	⋯	⋯	⋯	⋯	⋯	−3.2
KOI-2418	2456177.9199	19.4	⋯	⋯	⋯	⋯	⋯	⋯	+5.4
KOI-2626	2456179.8154	17.3	⋯	⋯	⋯	⋯	⋯	⋯	−2.5
KOI-2650	2456166.9364	17.7	⋯	⋯	⋯	⋯	⋯	⋯	−22.4
KOI-3010	2456208.8892	19.5	⋯	⋯	⋯	⋯	⋯	⋯	+0.7
KOI-3282	2456880.9972	13.6	⋯	⋯	⋯	⋯	⋯	⋯	−2.1
KOI-3497	2456508.0625	90.0	⋯	⋯	⋯	⋯	⋯	⋯	−17.9
KOI-4036	2456588.8874	46.7	⋯	⋯	⋯	⋯	⋯	⋯	−20.7
KOI-4054	2457265.8981	36.9	⋯	⋯	⋯	⋯	⋯	⋯	−25.6
KOI-4356	2456882.0965	12.9	⋯	⋯	⋯	⋯	⋯	⋯	+8.6
KOI-4450	⋯	⋯	⋯	⋯	2456589.6857	16.9	2456536.7629	32.0	−44.9
KOI-4550	⋯	⋯	⋯	⋯	⋯	⋯	2456536.7130	26.5	⋯
KOI-5236	2457265.0439	56.3	2456934.6175	32.6	⋯	⋯	⋯	⋯	−31.5
KOI-5856	⋯	⋯	⋯	⋯	2456814.7854	23.7	⋯	⋯	−94.3

other hand, that the centroid offsets in Table 3 were computed assuming that the host stars do not have close companions of similar brightness ($\rho < 4''$, $\Delta m \lesssim 2$ mag). However, as seen in Table 2, several of our targets do have such companions, which can introduce error in the centroid measurements. To be conservative, we doubled the size of the offset uncertainties, and therefore of the 3σ exclusion regions for those cases. These instances are indicated in Table 3.

4.3. Spectroscopic Observations

Many of our targets have been observed spectroscopically as part of the Exoplanet Follow-up Observing Program for *Kepler*. A variety of instruments and telescopes have been used, including HIRES (Vogt et al. 1994) on the 10 m Keck I telescope on Maunakea (Hawaii) with a typical resolving power of $R \approx 60{,}000$, TRES (Fűrész 2008) on the 1.5 m Tillinghast reflector at the Fred L. Whipple Observatory (Arizona) with $R \approx 44{,}000$, the Tull spectrograph (Tull et al. 1995) on the 2.7 m McDonald Observatory telescope (Texas) with $R \approx 60{,}000$, and the RCSpec instrument (see Everett et al. 2013) on the 4 m Kitt Peak National Observatory telescope (Arizona) with $R \approx 3000$. The reduced observations are available on the ExoFOP Web page, and we list them in Table 4 with their barycentric Julian dates of observation (BJD), S/N per resolution element, and measured heliocentric radial velocities. Additionally, several of the cooler targets have been observed in the near-infrared by others, including Muirhead et al. (2012, 2014), Mann et al. (2013a, 2013b), and Newton et al. (2015). Details of the instrumentation and reduction procedures for those observations may be found there.

All of the optical and near-infrared spectra appear single lined. To aid in ruling out potential false positives that could be causing the transit signals, the 15 targets with available Keck/HIRES observations (i.e., all except for KOI-4450, 4550, and 5856) were subjected to injection/recovery simulations to determine limits to the brightness of potential stellar companions that may fall within the slit of the HIRES instrument, which has a typical half width of $0\farcs43$. For details of the procedure, we refer the reader to the work of Kolbl et al. (2015). We find that in general we should be able to detect companions brighter than about 1% of the flux of the target star ($\Delta m = 5$ mag) provided the line separation is more than 10 km s^{-1} in velocity space. For smaller separations, we assume the line blending would prevent detection of any companions. For the coolest stars and for targets with lower S/N spectra, the limits are not as strong, and we are only able to detect companions down to about 3% of the flux of the primary star ($\Delta m = 3.8$ mag) at velocity separations larger than 20 km s^{-1}. This is the case for KOI-0172, 0463, 2626, 2650, 3282, 3497 (10 km s^{-1} limit), and 4356. For KOI-4450, 4550, and 5856, we adopted a brighter threshold corresponding to $\Delta m = 2$ mag (16% relative flux) and assumed that any spectroscopic companions would escape detection if their radial velocity is within 30 km s^{-1} of that of the main target.

5. Stellar Properties

The atmospheric properties of the host stars, including the effective temperature, surface gravity, and metallicity ($T_{\rm eff}$, $\log g$, [Fe/H]), are key inputs to infer their absolute mass and radius, which we describe below. Here, we derived the atmospheric properties using several methods depending on the spectra available. For the Keck/HIRES spectra, we applied two different procedures. One is a version of the `Spec-Match-Emp` algorithm (Yee et al. 2017)[19] that compares an observed spectrum against a large library of observed spectra of well-characterized stars obtained with the same instrument and finds the best match. This procedure works well for solar-type stars but degrades below $T_{\rm eff} \sim 4300$ K because such stars are not as well-represented in the reference library used for this work. The other procedure applied to the Keck observations is `SPC` (Buchhave et al. 2012), which uses a cross-correlation technique to compare a region centered on the Mg I b triplet (∼5187 Å) in the observed spectrum against a grid of synthetic templates based on model atmospheres by R. L. Kurucz. The same `SPC` procedure was applied to the TRES spectra,

[19] https://github.com/samuelyeewl/specmatch-emp

Table 5
Spectroscopic Properties and Age Constraints for the Targets

Star	$T_{\rm eff}$ (K)	[Fe/H] (dex)	$\log g$ (cm s^{-2})	$P_{\rm rot}$[a] (days)	Gyro Age (Gyr)	$T_{\rm eff}$ Source	[Fe/H] Source	$\log g$ Source	$P_{\rm rot}$ Source
KOI-0172	5700 ± 100	-0.10 ± 0.10	4.34 ± 0.10	⋯	⋯	1, 3	1, 3	1, 3	⋯
KOI-0438	4057^{+251}_{-64}	-0.33 ± 0.11	⋯	26.43	$2.9^{+0.3}_{-0.3}$	6	6	⋯	11, 13, 15
KOI-0463	3430 ± 48	-0.25 ± 0.06	⋯	50.47	$6.5^{+1.9}_{-1.2}$	7, 9, 10	7, 8	⋯	12, 13
KOI-0812	3996 ± 55	-0.51 ± 0.06	⋯	39.49	$5.8^{+0.5}_{-0.2}$	7, 9	7, 8	⋯	11, 13
KOI-0854	3674 ± 40	$+0.21 \pm 0.05$	⋯	20.09	$1.4^{+0.7}_{-0.3}$	7, 9, 10	7, 8	⋯	11, 12, 13, 15
KOI-2418	3577 ± 58	$+0.16 \pm 0.08$	⋯	17.63	$1.2^{+0.7}_{-0.3}$	9	8	⋯	11, 12, 13, 15
KOI-2626	3638 ± 51	-0.30 ± 0.12	⋯	31.18	$3.2^{+0.7}_{-0.8}$	7, 9	7, 8	⋯	11
KOI-2650	3931 ± 47	-0.02 ± 0.09	⋯	19.92	$1.5^{+0.6}_{-0.3}$	7, 9, 10	7, 8	⋯	11, 12, 13, 15
KOI-3010	3950 ± 56	$+0.04 \pm 0.12$	⋯	14.09	$0.8^{+0.6}_{-0.2}$	7, 9	7	⋯	11, 13, 14, 15
KOI-3282	3950 ± 113	-0.21 ± 0.11	⋯	18.32	$1.3^{+0.5}_{-0.2}$	7, 10	7	⋯	12, 14, 15
KOI-3497	3484 ± 91	$+0.15 \pm 0.11$	⋯	∼10	$1.0^{+1.0}_{-0.5}$	7	7	⋯	16
KOI-4036	4820 ± 100	-0.08 ± 0.10	4.54 ± 0.10	⋯	⋯	1, 2	1, 2	1, 2	⋯
KOI-4054	5276 ± 100	$+0.06 \pm 0.10$	4.62 ± 0.10	⋯	⋯	1, 2	1, 2	1, 2	⋯
KOI-4356	4745 ± 100	-0.10 ± 0.10	4.54 ± 0.10	⋯	⋯	2	2	2	⋯
KOI-4450	5461 ± 100	$+0.12 \pm 0.10$	4.45 ± 0.15	⋯	⋯	4	4	4	⋯
KOI-4550	4807 ± 100	-0.18 ± 0.10	4.45 ± 0.15	⋯	⋯	4	4	4	⋯
KOI-5236	5995 ± 50	-0.23 ± 0.08	4.30 ± 0.10	⋯	⋯	1, 2, 3	1, 2, 3	1, 2, 3	⋯
KOI-5856	5906^{+183}_{-147}	$-0.76^{+0.32}_{-0.26}$	$4.47^{+0.10}_{-0.29}$	⋯	⋯	5	5	5	⋯

Note. Sources in the last four columns are (1) Keck/HIRES spectrum analyzed with `SPC`, (2) Keck/HIRES spectrum analyzed with `SpecMatch-Emp`, (3) TRES spectrum analyzed with `SPC`, (4) KPNO spectrum analyzed as described by Everett et al. (2013), (5) Huber et al. (2014), (6) Muirhead et al. (2012), (7) Muirhead et al. (2014), (8) Mann et al. (2013b), (9) Mann et al. (2013a), (10) Newton et al. (2015), (11) Walkowicz & Basri (2013), (12) McQuillan et al. (2013a), (13) McQuillan et al. (2013b), (14) Nielsen et al. (2013), (15) Reinhold et al. (2013), (16) see text.
[a] Uncertainties are assumed to be 5%.

although the smaller telescope and use of a narrow wavelength range limited this to the brighter stars. Results for the McDonald Observatory spectra were obtained using the `Kea` analysis tool (Endl & Cochran 2016), and the KPNO spectra were analyzed with the procedures described by Everett et al. (2013). Both of these methods rely on libraries of synthetic spectra.

For stars hotter than 4300 K, we took an average of all available results and we report them in Table 5 along with the sources. For KOI-5856, the parameters resulting from the `Kea` analysis provide a less satisfactory fit to the McDonald spectrum than those reported by Huber et al. (2014); we therefore adopted the latter, along with their considerably larger formal uncertainties. For KOI-0172, the `SpecMatch-Emp` analysis converged on a subgiant classification ($\log g = 3.82$) as well as a significantly cooler temperature and lower metallicity than two other determinations that are based on spectra from two different telescopes favoring a main-sequence classification. We adopted the main-sequence results.

For the cooler stars, we preferred to rely on results from the literature based on near-infrared spectra, as the techniques based on optical spectra tend to break down for late K and M stars. Infrared determinations of $T_{\rm eff}$ and [Fe/H] use various spectral indices and calibrations developed in recent years (see Rojas-Ayala et al. 2012; Terrien et al. 2012; Mann et al. 2013a, 2013b; Newton et al. 2015), although there are still some differences among different methods. For example, Mann et al. (2013a) indicate that their temperatures are on average 72 K hotter than those of Muirhead et al. (2012), which use the Rojas-Ayala et al. (2012) calibration. On the other hand, Newton et al. (2015) claim that their temperatures are essentially on the same scale as those of Mann et al. (2013a) (with only a 10 K difference), which seems to be confirmed by the fact that both sets of authors claim their respective scales are some 40 K hotter than those of Dressing & Charbonneau (2013). The latter determinations are photometric rather than spectroscopic, but can nevertheless serve as a secondary reference. Some of our stars have also been classified by Muirhead et al. (2014), whose temperatures are on the same scale as those of Muirhead et al. (2012) given that they use the same calibrations. To refer all temperatures to the same scale, we chose to adjust the Muirhead et al. (2012, 2014) values for our targets by +72 K to place them on the same scale as the Mann/Newton temperatures. We note also that some of the results by Muirhead et al. (2012) have been superseded by those of Muirhead et al. (2014), who used the same spectra.

Several of the above studies report metallicity determinations for the KOIs in our sample, sometimes in the form of [m/H] indices (Muirhead et al. 2012), other times as [Fe/H] indices (Mann et al. 2013b), and occasionally both (Muirhead et al. 2014). These measures have sometimes been used interchangeably in the literature. We note, however, that [m/H] and [Fe/H] are not the quite same and are typically not independent in the above studies. Published [m/H] results by these authors are based on a calibration by Rojas-Ayala et al. (2012), and a close look reveals a perfectly linear relation between that [m/H] calibration and a similar one by the same authors for [Fe/H]. This is traceable to a similar relation present between [m/H] and [Fe/H] in the metallicity estimates of many of the standard stars used by Rojas-Ayala et al. (2012), which come from the work of Valenti & Fischer (2005). Consequently, for this work, we uniformly used [Fe/H] when both are available from the same source (as in the study by Muirhead et al. 2014), and when only [m/H] is available we converted it to [Fe/H] using the Rojas-Ayala et al. (2012) relations.

For the cool stars in our sample, we adopted weighted averages of all available near-infrared determinations of $T_{\rm eff}$

and [Fe/H]. These are also reported in Table 5 with their sources.

A comparison of the spectroscopic properties in Table 5 with the values in the catalog of Mathur et al. (2017), which was used for the final transiting planet search run by the *Kepler* Mission (DR25), indicates a few significant differences. For KOI-4356 and KOI-5856, our temperatures are ∼400 K hotter and our metallicities differ by +1.4 and −1.0 dex from DR25. For KOI-4356, we suspect this is because the DR25 estimates are photometric, whereas ours are spectroscopic. For KOI-5856, we are not able to trace the source of the DR25 determinations in the published literature at the time of this writing and chose to revert to the values reported by Huber et al. (2014), as explained earlier. For KOI-4550 and KOI-5236, our spectroscopic metallicities are lower by about 0.34 dex, with the DR25 values being from the same unpublished source indicated above.

Unlike optical determinations for solar-type stars, near-infrared spectroscopic analyses of cool stars are typically not able to provide a measure of the surface gravity, which has a relatively subtle effect on the line profiles. Consequently, when attempting to infer the stellar properties by comparison with model isochrones as described below, there is no handle on the radii (or age) of these objects, which then hampers the determination of the planetary radii. The sizes of cool stars change relatively little with age, so in the end, this uncertainty is not very important. Nevertheless, following Torres et al. (2015), we took advantage of the fact that all of these cool stars show periodic brightness variations that we interpret as due to rotational modulation caused by spots. We use the measured rotation periods ($P_{\rm rot}$) for these stars along with gyrochronology relations to estimate a rough age, which in turn serves to constrain the isochrone fits and enables us to infer a radius. The rotation period estimates are averages from the work of Walkowicz & Basri (2013), McQuillan et al. (2013a, 2013b), Nielsen et al. (2013), and Reinhold et al. (2013), which agree fairly well with each other for objects in common. The average periods are listed with their sources in Table 5 and are assumed to have uncertainties of 5%. To infer ages, we used the gyrochronology relations by Epstein & Pinsonneault (2014). The required $B - V$ color indices were adopted either from the *UBV* survey of the *Kepler* field by Everett et al. (2012)[20] or from the AAVSO Photometric All-Sky Survey (APASS; Henden et al. 2012) for KOI-0438, and were corrected for the presence of the close companions reported in Section 4.1 on the assumption that they are physically associated. Reddening corrections were made using the reddening values listed in the *Kepler* Input Catalog (KIC; Brown et al. 2011). To account for possible errors in these adjustments, we adopted a conservative uncertainty of 0.10 mag for the dereddened $B - V$ colors. The ages derived in this way are presented also in Table 5. Although there is no published rotation period for KOI-3497, its raw light curve shows a rather clear periodicity near 10 days, similar to that of Hyades stars of its spectral type, which suggests a relatively young age. We assign it an age of $1.0^{+1.0}_{-0.5}$ Gyr with a generous uncertainty.

With these spectroscopic properties and age constraints for the cooler objects, we estimated the physical properties of all our targets (most importantly the mass and radius) using stellar evolution models from the Dartmouth series (Dotter et al. 2008). We employed a Monte Carlo procedure in which we perturbed each of the three observational constraints assuming they follow uncorrelated Gaussian distributions characterized by the errors reported in Table 5. We generated half a million such sets, and for each one, we obtained the best fit to the model isochrones based on a standard χ^2 criterion involving the three observables and their uncertainties. The analysis was based on a pre-computed grid of models with a metallicity resolution of 0.01 dex, sufficient for our purposes, and an age resolution of 0.5 Gyr up to 13.5 Gyr (0.25 Gyr for ages younger than 4 Gyr), with linear interpolation for intermediate-age values. Masses were explored along each isochrone on a fine grid generated by cubic spline interpolation with a step equal to 1/1000th of the separation between consecutive mass values in the original isochrone tables. Once the best fit was identified, other properties including the radii, stellar densities, bolometric luminosities, and passband-specific absolute magnitudes were calculated or simply read off of the isochrone, with cubic spline interpolation at the best-fit mass, as needed. We collected the outcome of these simulations into distributions for the stellar properties of interest and adopted the mode of each distribution as a representative value. In all cases, the distributions were unimodal. The results are presented in Table 6, where the uncertainties correspond to the 68.3% (1σ) credible intervals. Distances were calculated from the absolute K_s magnitudes derived from the isochrone fits along with the apparent brightness from the Two Micron All-Sky Survey (2MASS; Cutri et al. 2003) in the same passband, which is the one least affected by interstellar extinction. We made appropriate corrections for extinction, as well as for the presence of unresolved companions, as above.

6. Candidate Validation

The faintness of our targets combined with the very small Doppler signals expected for Earth-size planets in relatively long-period orbits typically prevents confirmation of their planetary nature by the radial-velocity technique. The alternative is statistical validation, whose goal is to show that the likelihood of a true planet is much greater than that of a false positive. Here, we applied the BLENDER technique (Torres et al. 2004, 2011, 2015), which has been used previously to validate many of the most iconic results from the *Kepler* Mission (see, e.g., Fressin et al. 2012; Barclay et al. 2013; Borucki et al. 2013; Meibom et al. 2013; Kipping et al. 2014, 2016; Jenkins et al. 2015). BLENDER relies on the information contained in the shape of the transit light curve to help rule out astrophysical false positives. The types of false positives considered by BLENDER include blends with eclipsing binaries as well as with single stars transited by a (larger) planet. In both cases, the intruding binary system may be in the background, in the foreground, or even physically bound to the target star. Other ingredients in the calculations include known distributions of binary star properties (periods, eccentricities, mass ratios, etc.), the number density of stars in the vicinity of each KOI from Galactic structure models, and the estimated rates of occurrence of eclipsing binary stars and transiting planets as determined from the *Kepler* Mission itself.

As noted in the Introduction, many of the KOIs in our sample have been validated with other methodologies and have received official *Kepler* designations as reported in Table 1. Three that are in multicandidate systems ("multis"), KOI-0438.02, KOI-0812.03, and KOI-2650.01, were announced as

[20] A correction of +0.10 mag was applied to the V magnitudes to bring them onto the standard system.

Table 6
Physical Properties of the Targets Derived from Isochrone Fits

Star	Age (Gyr)	$M_\star$ ($M_\odot$)	$R_\star$ ($R_\odot$)	$\log g$ (cm s^{-2})	$\rho_\star$ ($\rho_\odot$)	$\log L_\star$ ($L_\odot$)	M_V (mag)	M_{K_s} (mag)	Distance (pc)
KOI-0172	$9.8^{+1.7}_{-4.1}$	$0.914^{+0.051}_{-0.039}$	$0.991^{+0.151}_{-0.072}$	$4.399^{+0.070}_{-0.106}$	$0.85^{+0.31}_{-0.23}$	$-0.021^{+0.134}_{-0.087}$	$4.89^{+0.23}_{-0.34}$	$3.33^{+0.18}_{-0.31}$	595^{+95}_{-45}
KOI-0438	$2.9^{+0.4}_{-0.3}$	$0.542^{+0.053}_{-0.125}$	$0.529^{+0.045}_{-0.135}$	$4.721^{+0.147}_{-0.027}$	$4.11^{+2.73}_{-0.96}$	$-1.210^{+0.186}_{-0.388}$	$8.78^{+1.28}_{-0.66}$	$5.34^{+0.88}_{-0.39}$	195^{+52}_{-58}
KOI-0463	$6.8^{+1.9}_{-1.2}$	$0.269^{+0.046}_{-0.039}$	$0.272^{+0.040}_{-0.031}$	$4.995^{+0.042}_{-0.047}$	$12.73^{+3.76}_{-2.36}$	$-2.022^{+0.129}_{-0.143}$	$11.44^{+0.44}_{-0.37}$	$7.21^{+0.34}_{-0.31}$	69^{+12}_{-9}
KOI-0812	$6.0^{+0.6}_{-0.3}$	$0.507^{+0.019}_{-0.023}$	$0.495^{+0.020}_{-0.026}$	$4.753^{+0.027}_{-0.018}$	$4.14^{+0.54}_{-0.29}$	$-1.253^{+0.059}_{-0.074}$	$8.85^{+0.23}_{-0.20}$	$5.48^{+0.17}_{-0.13}$	331^{+23}_{-23}
KOI-0854	$1.6^{+0.8}_{-0.3}$	$0.534^{+0.019}_{-0.022}$	$0.502^{+0.018}_{-0.021}$	$4.763^{+0.020}_{-0.015}$	$4.18^{+0.42}_{-0.26}$	$-1.385^{+0.050}_{-0.060}$	$9.76^{+0.20}_{-0.18}$	$5.62^{+0.14}_{-0.12}$	321^{+20}_{-20}
KOI-2418	$1.5^{+0.8}_{-0.2}$	$0.480^{+0.030}_{-0.046}$	$0.450^{+0.029}_{-0.041}$	$4.811^{+0.042}_{-0.026}$	$5.21^{+1.14}_{-0.58}$	$-1.533^{+0.084}_{-0.114}$	$10.24^{+0.33}_{-0.29}$	$5.98^{+0.28}_{-0.20}$	194^{+21}_{-22}
KOI-2626	$3.2^{+0.7}_{-0.8}$	$0.404^{+0.040}_{-0.047}$	$0.382^{+0.036}_{-0.040}$	$4.878^{+0.046}_{-0.036}$	$7.05^{+1.90}_{-0.98}$	$-1.638^{+0.093}_{-0.122}$	$10.22^{+0.35}_{-0.28}$	$6.32^{+0.30}_{-0.23}$	252^{+32}_{-30}
KOI-2650	$1.6^{+0.7}_{-0.3}$	$0.578^{+0.022}_{-0.023}$	$0.549^{+0.021}_{-0.022}$	$4.721^{+0.018}_{-0.017}$	$3.47^{+0.32}_{-0.23}$	$-1.194^{+0.057}_{-0.055}$	$8.85^{+0.20}_{-0.17}$	$5.27^{+0.12}_{-0.15}$	339^{+26}_{-18}
KOI-3010	$1.3^{+0.6}_{-0.1}$	$0.594^{+0.027}_{-0.029}$	$0.566^{+0.021}_{-0.031}$	$4.704^{+0.029}_{-0.010}$	$3.25^{+0.43}_{-0.17}$	$-1.158^{+0.058}_{-0.073}$	$8.79^{+0.23}_{-0.22}$	$5.10^{+0.24}_{-0.07}$	436^{+32}_{-33}
KOI-3282	$1.4^{+0.6}_{-0.2}$	$0.544^{+0.036}_{-0.047}$	$0.518^{+0.039}_{-0.048}$	$4.744^{+0.045}_{-0.034}$	$3.89^{+0.89}_{-0.53}$	$-1.247^{+0.123}_{-0.133}$	$8.94^{+0.46}_{-0.40}$	$5.43^{+0.28}_{-0.32}$	309^{+53}_{-35}
KOI-3497	$1.6^{+1.0}_{-0.3}$	$0.418^{+0.051}_{-0.090}$	$0.393^{+0.048}_{-0.072}$	$4.865^{+0.077}_{-0.045}$	$6.76^{+3.18}_{-1.30}$	$-1.695^{+0.132}_{-0.228}$	$10.74^{+0.67}_{-0.42}$	$6.37^{+0.55}_{-0.32}$	81^{+15}_{-17}
KOI-4036	$3.9^{+7.3}_{-0.8}$	$0.743^{+0.034}_{-0.030}$	$0.713^{+0.031}_{-0.025}$	$4.608^{+0.017}_{-0.032}$	$2.06^{+0.17}_{-0.20}$	$-0.606^{+0.071}_{-0.067}$	$6.64^{+0.24}_{-0.23}$	$4.27^{+0.10}_{-0.12}$	331^{+19}_{-15}
KOI-4054	$3.0^{+6.6}_{-0.5}$	$0.863^{+0.040}_{-0.037}$	$0.817^{+0.051}_{-0.030}$	$4.557^{+0.020}_{-0.056}$	$1.58^{+0.16}_{-0.24}$	$-0.333^{+0.077}_{-0.067}$	$5.76^{+0.21}_{-0.21}$	$3.85^{+0.11}_{-0.15}$	591^{+43}_{-28}
KOI-4356	$3.4^{+7.8}_{-0.3}$	$0.725^{+0.034}_{-0.029}$	$0.698^{+0.029}_{-0.025}$	$4.616^{+0.017}_{-0.030}$	$2.14^{+0.18}_{-0.19}$	$-0.652^{+0.070}_{-0.068}$	$6.80^{+0.25}_{-0.23}$	$4.33^{+0.11}_{-0.11}$	657^{+39}_{-33}
KOI-4450	$9.4^{+1.9}_{-5.8}$	$0.921^{+0.044}_{-0.040}$	$0.915^{+0.117}_{-0.051}$	$4.486^{+0.041}_{-0.107}$	$1.19^{+0.22}_{-0.34}$	$-0.171^{+0.125}_{-0.076}$	$5.30^{+0.22}_{-0.33}$	$3.57^{+0.13}_{-0.28}$	914^{+126}_{-58}
KOI-4550	$7.7^{+3.6}_{-4.6}$	$0.719^{+0.035}_{-0.029}$	$0.693^{+0.030}_{-0.024}$	$4.618^{+0.017}_{-0.031}$	$2.16^{+0.18}_{-0.20}$	$-0.636^{+0.071}_{-0.066}$	$6.73^{+0.24}_{-0.23}$	$4.33^{+0.10}_{-0.12}$	755^{+44}_{-36}
KOI-5236	$7.6^{+1.1}_{-2.5}$	$0.959^{+0.037}_{-0.035}$	$1.075^{+0.174}_{-0.081}$	$4.335^{+0.087}_{-0.102}$	$0.66^{+0.31}_{-0.16}$	$+0.130^{+0.131}_{-0.077}$	$4.50^{+0.19}_{-0.33}$	$3.09^{+0.18}_{-0.32}$	521^{+86}_{-39}
KOI-5856	$5.7^{+5.1}_{-2.6}$	$0.817^{+0.092}_{-0.048}$	$0.835^{+0.189}_{-0.075}$	$4.525^{+0.052}_{-0.165}$	$1.40^{+0.41}_{-0.58}$	$-0.114^{+0.210}_{-0.120}$	$5.14^{+0.32}_{-0.54}$	$3.69^{+0.21}_{-0.48}$	764^{+186}_{-77}

Note. Values correspond to the mode of the corresponding parameter distributions, with 68.3% credible intervals (see text).

validated by Rowe et al. (2014) based on the statistical argument that planet-like signals in multis have a very high chance of being caused by true planets (Lissauer et al. 2014). Ten others received *Kepler* designations after being validated with the algorithm known as VESPA (Morton et al. 2016),[21] which adds up the likelihoods of different types of false-positive scenarios and compares them with that of a planet. VESPA has also been applied to the rest of our targets, though not all have been considered validated. In both of these techniques, the main false positives considered are those that involve eclipsing binaries. Scenarios in which the planet transits an unseen star in the photometric aperture rather than the intended target, and is therefore larger than it appears, are not considered to be false positives in those methods as they are only concerned with demonstrating the presence of a planet along the line of sight to the target, regardless of its size or exact location. The typical threshold for validation in these methods is a confidence level of 99%.

Here we are interested in confirming planets that have a chance of being habitable, so the situation is different in that the size of the planetary body is just as important as the flux it receives from the parent star. This is because planets much larger than about 1.8 $R_\oplus$ are more likely to be gaseous than rocky, and may lack a solid surface to support liquid water (e.g., Rogers 2015; Wolfgang et al. 2016; Fulton et al. 2017). Therefore, the chance that the planet is around a star different from the intended target, and is thus larger than it appears, must be taken into account for the validation. As we demonstrate below, these kinds of false positives tend to dominate the overall blend frequency, and including them in the analysis makes validations significantly more challenging. For this reason, we consider the previous validations of most of our targets to be insufficient for our purposes, and we revisit them with BLENDER. Additionally, we chose to be more conservative given the importance of these objects, and we adopt a higher threshold for validation corresponding to a 99.73% confidence level (3σ), consistent with previous applications of BLENDER.

Finally, another of our targets (KOI-0172.02) was considered validated by Barclay et al. (2013) at the 99.3% confidence level using a scheme somewhat similar to BLENDER, though with more simplified assumptions. We revisit this case as well.

Full details of the BLENDER procedure have been described in many of the previous applications of this technique, as listed at the beginning of this section, most recently by Torres et al. (2015). We summarize the principles here for the benefit of the reader. For each KOI, BLENDER first simulates a large number of realistic false-positive scenarios involving eclipsing binaries as well as larger planets transiting blended stars, and compares the synthetic light curves for each of them against the *Kepler* light curves in a χ^2 sense. The properties of the stars involved in blends are derived based on model isochrones. The simulated transit light curves account for any extra light in the aperture, such as that coming from the close companions reported in Section 4.1. Blends that result in the wrong shape for the transit are considered to be ruled out. This allows us to place useful constraints on the properties of the objects making up the blend, including their sizes and masses, their color and brightness, the line-of-sight distance between the eclipsing pair and the KOI, the eccentricities of the orbits, etc. Monte Carlo simulations are then performed to estimate the frequencies of blends of different kinds allowed by the above exploration of parameter space and accounting also for all additional constraints coming from the follow-up observations (see below). Finally, the total blend frequency is compared with the expected frequency of planets of the period and size implied by the observations (referred to here as the "planet prior") to infer the confidence level of the validation.

To help in the rejection of blends, we made use of contrast curves from the high-resolution imaging for each KOI, which

[21] https://github.com/timothydmorton/VESPA

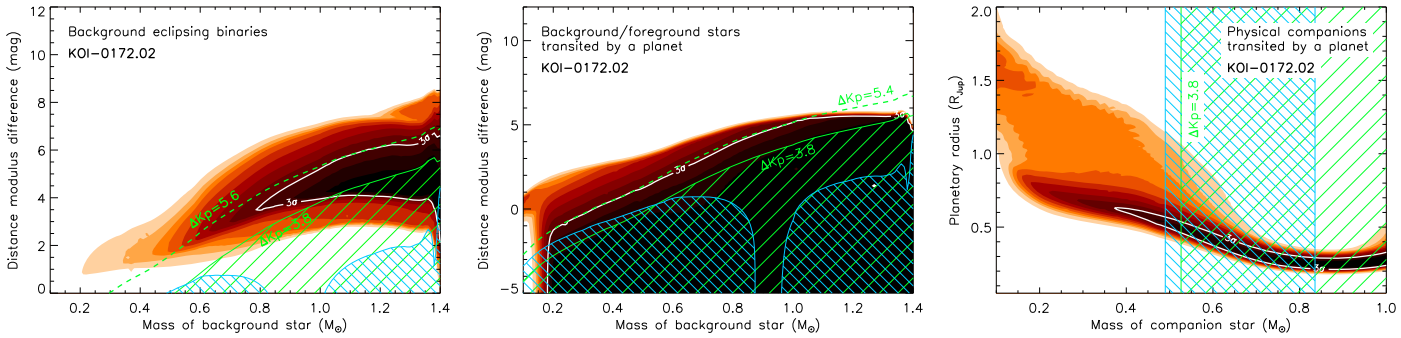

Figure 2. Map of the χ^2 surface (goodness of fit) for KOI-0172.02 for three different blend scenarios, as labeled. Only blends within the solid white contours (darker shading) provide fits to the *Kepler* light curves that are within acceptable limits (3σ, where σ is the significance level of the χ^2 difference compared to a transiting planet model fit; see Fressin et al. 2012). Other concentric colored areas (lighter colors) represent fits that are increasingly worse (4σ, 5σ, etc.), which we consider to be ruled out. The hatched green areas indicate regions of parameter space where blended stars can be excluded if they are within $0\farcs43$ of the target (half-width of the spectrometer slit), within 3.8 mag in brightness (3% relative flux), and have a radial velocity differing from the target by 20 km s^{-1} or more. In all of those cases, they would have been detected spectroscopically. Blends in the hatched blue areas can also be ruled out because they would be either too red (left) or too blue (right), by more than three times the measurement uncertainty, compared to the measured $r - K_s$ color of KOI-0172.02. Left: BEB scenario. The vertical axis represents the linear distance between the eclipsing binary and the target ($D_{\rm BEB}$–$D_{\rm targ}$), cast for convenience in terms of the distance modulus difference $\Delta\delta = 5\log(D_{\rm BEB}/D_{\rm targ})$. Eclipsing binaries with primary stars above the dashed green line ($\Delta Kp = 5.6$ mag) are too faint to mimic the transit. Middle: BP scenarios. The combination of the $r - K_s$ color constraint and the spectroscopic constraint rules out many of the otherwise viable blends. Right: HTP scenario. The vertical axis now shows the size of the planet transiting the companion star, in units of Jupiter's radius. All blends of this kind within 3.8 mag of the target are excluded, and others are also ruled out for being too blue. Only physical companions below 0.49 $M_\odot$ can still mimic the *Kepler* light curve and go undetected.

provides information on the detectability of close companions as a function of the angular separation from the target. Similarly, our high-resolution spectroscopy places limits on the brightness of companions falling within the slit of the spectrograph that would be seen as a second set of spectral lines, if separated enough from the lines of the target (Section 4.3). The centroid motion analysis is able to exclude blended objects beyond a certain angular separation (the 3σ exclusion regions reported in Section 4.2), regardless of brightness. Finally, we used the observed $r - K_s$ color of the KOI as listed in the KIC to eliminate blends that are too red or too blue by more than three times the observational uncertainties compared to the target.

6.1. Results

In the following, we refer to blend scenarios involving background or foreground eclipsing binaries as "BEB." Blends with a background or foreground star transited by a larger planet are denoted "BP." Physically associated stars transited by another star or by a planet (hierarchical triple configurations) are referred to as "HTS" and "HTP," respectively.

We illustrate the constraints derived from the shape of the light curve and the follow-up observations using KOI-0172.02 as an example. Figure 2 shows cross-sections of parameter space for blends from three different scenarios: BEB, BP, and HTP. We find that no HTS scenario results in acceptable fits to the *Kepler* photometry for this candidate, or indeed for any of the other stars in our sample. For the BEB scenario (left panel), `BLENDER` indicates that eclipsing binaries constitute viable blends (darker region inside the white contour) only if the primary is a main-sequence star between about 0.8 and 1.4 $M_\odot$ (more massive stars will typically have evolved into a giant, producing the wrong shape for the transit), and is no fainter in the *Kepler* passband than 5.6 mag relative to the target. Also shown as hatched areas are sections of parameter space where blends can be ruled out based on constraints from spectroscopy (green) and $r - K_s$ color (blue). The vertical axis represents the distance between the binary and the target, expressed as a difference in distance modulus. A similar diagram for the BP scenario (middle panel) reveals that a background/foreground star transited by a planet can produce a signal mimicking the one observed for a wide range of masses between 0.2 and 1.4 $M_\odot$, provided it is within 5.4 mag of the brightness of the target. In this case, the observational constraints from spectroscopy and color remove large portions of parameter space. Finally, the right panel of Figure 2 shows that the allowed area of parameter space for the HTP configurations is a narrow swath in which the companion mass is larger than about 0.37 $M_\odot$ and the planet size is between 0.2 and 0.65 $R_{\rm Jup}$ (2.2–7.3 $R_\oplus$). However, much of this region is excluded either by the spectroscopic constraint or the color constraint.

Cross-sections of parameter space for the other KOIs are similar to those shown for KOI-0172.02, though we note that in one case (KOI-0463.01) `BLENDER` indicates that *all* blends involving background/foreground eclipsing binaries (BEB) or stars transited by a planet (HTP, BP) can be ruled out simply from the shape of the transit.

The blend frequencies obtained for each KOI and each type of false-positive scenario are presented in Table 7. The BEB quantities include the contribution from blended eclipsing binaries with equal primary and secondary eclipse depths and twice the orbital period, which is another potential source of confusion. As we indicated earlier, the overall blend frequency is seen to be dominated by the HTP scenarios (planet orbiting a physical companion to the target), which are typically two to three orders of magnitude more common than the other false-positive scenarios taken together. Also listed in the table are the expected planet priors ("PL"), the odds ratios defined as PL/(HTP + BP + BEB), and the statistical significance of the validations.

As mentioned above, for a 3σ validation (99.73% confidence level), we require a planet frequency that is at least $1/(1/99.73\% - 1) \approx 370$ times larger than the total blend frequency. All except for 3 of our 18 targets meet this threshold. KOI-4054.01, 4450.01, and 5236.01 are validated to somewhat lower confidence levels, though still above 99.4%. Two of the candidates, KOI-2626.01 and KOI-4550.01, are among those confirmed at the 99.73% confidence level or greater that had not been previously been validated. They are now given planet designations Kepler-1652b and Kepler-1653b, respectively (see

Table 7
Blend Frequencies, Planet Priors, Odds Ratios, and Significance Level of the Validations

Candidate	HTP	BP	BEB	PL	Odds Ratio	Significance	PL_{comp}	$\mathcal{P}$[targ]
KOI-0172.02	2.94E−07	5.71E−11	···	2.27E−04	772	99.87%	···	···
KOI-0438.02	6.32E−08	9.74E−12	5.88E−12	7.34E−05	1161	99.91%	···	···
KOI-0463.01	···	···	···	1.43E−05	···	100.00%	···	···
KOI-0812.03	1.65E−07	7.30E−12	···	2.31E−04	1400	99.93%	···	···
KOI-0854.01	1.03E−07	···	···	4.06E−05	394	99.75%	6.32E−05	39.1%
KOI-2418.01	···	1.41E−11	···	2.05E−04	···	100.00%	4.63E−06	97.8%
KOI-2626.01	9.89E−07	8.08E−10	1.83E−09	4.84E−04	488	99.80%	3.94E−04	55.2%
KOI-2650.01	6.01E−07	9.97E−10	1.20E−10	7.38E−04	1226	99.92%	···	···
KOI-3010.01	1.94E−07	4.74E−10	1.06E−10	4.10E−04	2107	99.95%	2.75E−04	59.9%
KOI-3282.01	1.58E−06	4.37E−10	1.05E−10	8.15E−04	516	99.81%	···	···
KOI-3497.01	···	3.48E−08	···	8.54E−04	24540	100.00%	5.18E−04	62.2%
KOI-4036.01	3.93E−07	3.40E−10	···	5.36E−04	1363	99.93%	···	···
KOI-4054.01	3.44E−07	7.15E−11	···	9.54E−05	277	99.64%	···	···
KOI-4356.01	1.97E−07	5.84E−10	3.01E−12	1.90E−04	962	99.90%	···	···
KOI-4450.01	3.06E−06	8.16E−09	1.22E−12	5.69E−04	185	99.46%	···	···
KOI-4550.01	5.07E−07	2.11E−09	1.80E−10	9.18E−04	1803	99.94%	8.29E−04	52.5%
KOI-5236.01	5.89E−07	1.56E−10	···	1.55E−04	263	99.62%	···	···
KOI-5856.01	8.74E−08	6.41E−11	···	3.16E−04	3613	99.97%	···	···

Note. For several of the candidates, the blend frequencies for the HTP, BP, and/or BEB scenarios are vanishingly small and are not reported. In eight cases in which the targets have a close companion detected from high-resolution imaging, we list the estimated planet frequency PL_{comp} assuming the planet transits the companion. For KOI-2626, which has two companions that can potentially mimic the transit light curve if transited by a planet, we added the corresponding frequencies. $\mathcal{P}$[targ] is the probability that the planet transits the target instead of a companion.

Table 1). For the remainder of the paper, we continue to refer to all validated planets by their KOI designations.

The validation results presented above are based on a comparison between the likelihood that the transit signals originate in the targets and the likelihood that they come from an unseen eclipsing object blended with the target. However, eight of our stars have one or more known close companions discovered with high-resolution imaging that cannot be excluded as the source of the signals by the centroid motion analysis described in Section 4.2. If the transit signals come from planets orbiting these companions, the size of the planet could be larger than it appears by a factor that depends on the physical size and brightness of the companion star.

Studies by Horch et al. (2014) and Hirsch et al. (2017) have concluded that the vast majority of sub-arcsecond companions to KOIs are bound to their primary stars. All but one of the companions to our targets are within 1″, the exception being the $\rho \approx 1\farcs94$ neighbor of KOI-5236, which is also the faintest of the ones not ruled out by the centroid motion analysis ($\Delta K \approx 6.4$ mag). For the seven companions that are within $0\farcs43$ (see Table 2), the conclusion that they are bound is further supported by the fact that we see no signs of these stars in the Keck/HIRES spectra even though they are all bright enough to have been discovered. This implies that their radial velocities must be similar to those of the targets, which argues for physical association. Under the assumption that companions within ∼1″ are bound, examination of the BLENDER constraints for the HTP scenario indicates that the $\rho \approx 0\farcs15$ neighbor of KOI-0854 can be excluded as a potential false positive because no planet transiting it can mimic the *Kepler* light curve well enough. The second companion to this KOI remains viable. For the $\rho \approx 1\farcs94$ companion to KOI-5236, the situation is less clear, as Hirsch et al. (2017) found that wider companions out to 2″ are about equally likely to be bound as unbound. However, the BLENDER constraints for both the HTP and the BP scenarios indicate that this star is too faint to be the source of the transit for any reasonable size planet. Thus, we are left with a total of six KOIs for which we cannot tell a priori whether the planet is around the target or one of the neighboring stars within about 1″.

To estimate the chance that the planet transits the KOI rather than a companion, we inferred the properties of the companions (size, brightness) using the same isochrone appropriate for the primary star and computed the planet prior in the same way as was done previously for the target, but this time assuming the planet is around the companion. The amount of dilution of the signal was adjusted accordingly to account for the larger contamination now coming from a brighter star in the aperture (the KOI). These planet frequencies are listed in Table 7 under the column labeled PL_{comp}. For the case of KOI-2626 with two close companions, we combined the companion planet frequencies. The chance that the planet is around the KOI as opposed to one of the companions was computed as $\mathcal{P}[\text{targ}] = PL/(PL + PL_{comp})$. In the case of KOI-2418.01, the statistics strongly suggest the planet indeed orbits the KOI; for the other five cases, we consider the results to be too close to 50% to be conclusive. The possibility remains, therefore, that the planets in these systems are larger than they appear, and we quantify this and discuss the implications in the next section.

7. Light-curve Fits and Planetary Parameters

The *Kepler* light curves of the KOIs, detrended as described in Section 3, were modeled following the procedure detailed in Section 4 of Rowe et al. (2014) that uses the analytic quadratic limb-darkening transit prescription of Mandel & Agol (2002). The technique is capable of handling systems with multiple transiting planets, fitting them simultaneously and parametrizing the transit model with the mean stellar density $\rho_\star$, on the assumption that all planets in a given system transit the same star and that their total mass is much smaller than that of the host star. For the three KOIs in our sample hosting multiple planets (KOI-0172, KOI-0438, KOI-0812), we further assumed non-interacting Keplerian orbits. Our model uses the quadratic

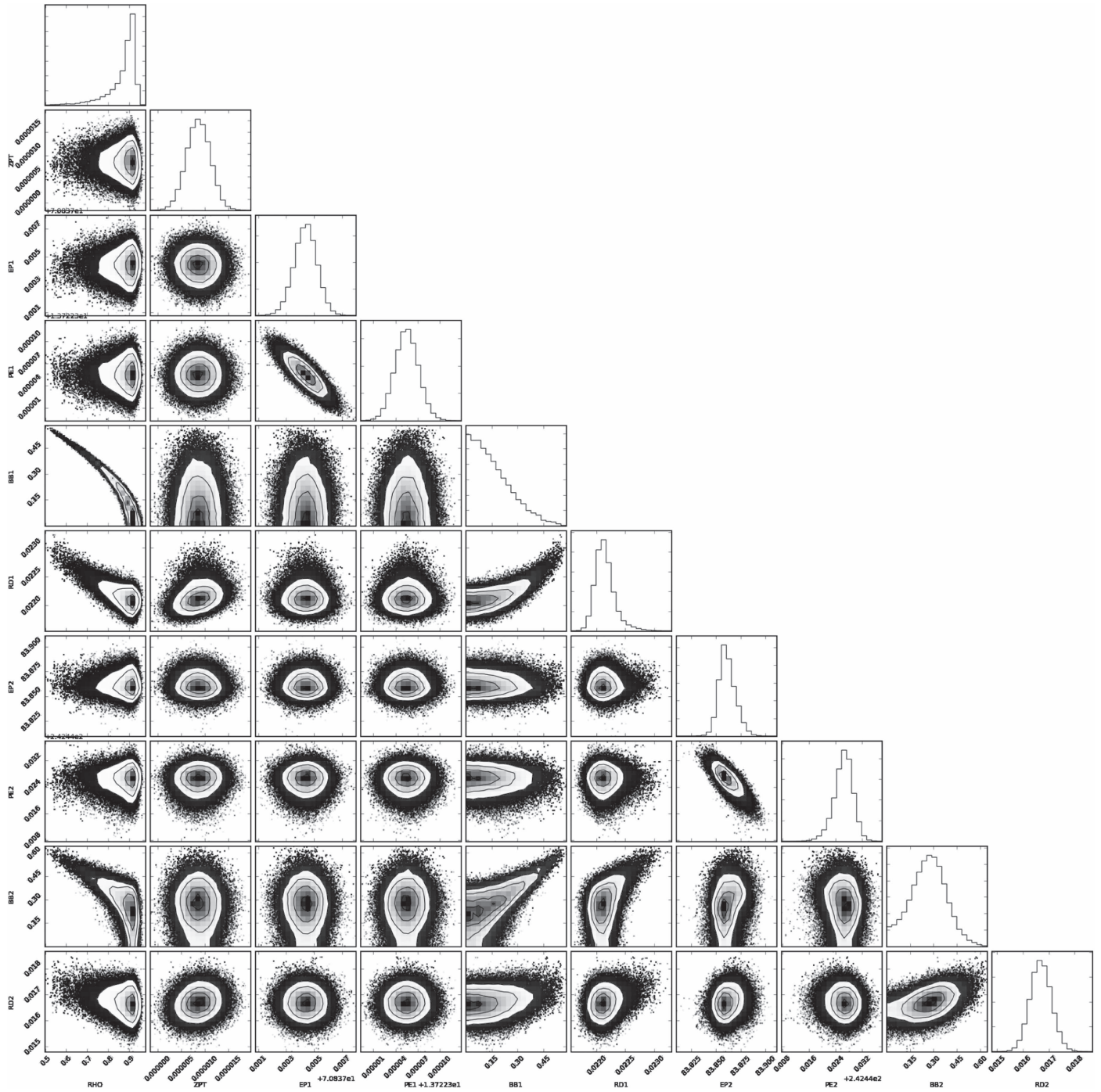

Figure 3. "Corner plot" (Foreman-Mackey 2016; https://github.com/dfm/corner.py) for the KOI-0172 multiplanet model fit illustrating the correlations among the fitted variables, for the case of circular orbits and fixed limb-darkening coefficients. Histogram panels represent the posterior distribution for each parameter. RHO is the mean stellar density ($\rho_\star$), ZPT is the photometric zero point, and EPX is the time of transit center, with X designating the modeled planet (1 or 2). PEX, BBX, and RDX are the orbital period (days), impact parameter (b), and scaled planetary radius ($R_p/R_\star$), respectively. Clear correlations among various parameters can be seen, such as that between $\rho_\star$ and b. The correlation between b for the two planets in the KOI-0172 system shows that the relative inclinations are better measured than absolute values.

limb-darkening reparametrization of Kipping (2013) with coefficients q_1 and q_2 to characterize the brightness profile of the host star. For each transiting planet n in a multiplanet system, we solved for the mean stellar density $\rho_\star$ (subject to a prior given by our spectroscopic work), the time of the first observed transit $T_{0,n}$, the orbital period P_n, a photometric zero point, the scaled planetary radius $(R_p/R_\star)_n$, the impact parameter b_n, and the shape parameters (e_n, ω_n) parametrized as $e_n \sin \omega_n$ and $e_n \cos \omega_n$.

To explore the impact of limb darkening and eccentricity on our measured model parameters, particularly on $R_p/R_\star$, we computed three sets of models:

1. Orbit assumed to be circular and limb-darkening coefficients held fixed based on the stellar properties listed in Table 6 and the limb-darkening tables of Claret & Bloemen (2011) for the *Kepler* bandpass;
2. Orbit assumed to be circular and limb-darkening coefficients solved for;

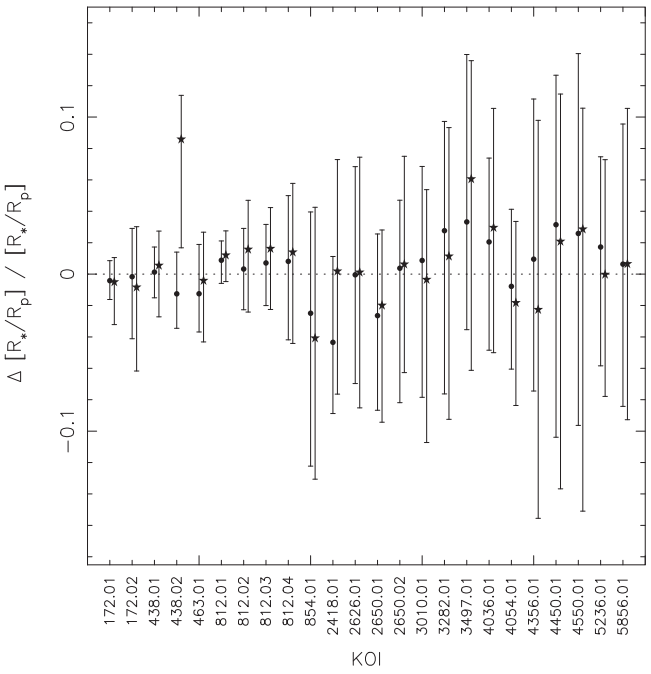

Figure 4. Fractional $R_p/R_\star$ differences and 1σ uncertainties between three alternate model fits for each KOI. Dots represent the difference between a model with fitted quadratic limb darkening (Model 2) and one with fixed quadratic limb-darkening parameters (Model 1), both with the eccentricity held at zero. Star symbols represent the difference between a model with the eccentricity and quadratic limb-darkening coefficients left free (Model 3) and a model with a circular orbit and fixed quadratic limb-darkening parameters (Model 1). In general, the uncertainty in $R_p/R_\star$ increases with model complexity, but in all cases the uncertainty in the stellar radius dominates the error budget. Most differences in $R_p/R_\star$ are consistent with zero. The largest excursion is seen for KOI-438.02, which weakly (less than 2σ confidence level) suggests either the detection of a slight eccentricity or a bias in our adopted $\rho_\star$ used as a prior.

3. Both the eccentricity and the limb-darkening coefficients considered as adjustable parameters.

For all three models, we used a prior on $\rho_\star$ based on the stellar properties presented in Table 6.

We obtained best-fit model parameters in each case using the code `TRANSITFIT5` (Rowe 2016), which implements a Levenberg–Marquardt χ^2 minimization routine (More et al. 1980). Posterior distributions of the model parameters were derived from a Markov Chain Monte Carlo (MCMC) analysis. The MCMC algorithm is similar to the approach described by Ford (2005) and Rowe et al. (2014). The program `TRANSITMCMC5` (Rowe 2016) was used to generate two Markov chains with lengths of 10^6. The first 10% of each chain was discarded as burn-in. A visual examination of the chains showed good mixture, and the Gelman–Rubin convergence criterion yielded R_c values of 1.01 or lower for all fitted parameters. Figure 3 displays histograms of the chain values for each parameter, and scatter plots to unveil potential correlations for the model parameter distributions in KOI-0172.02, for the case of $e = 0$ and fixed limb darkening. KOI-0172 has two known transiting planets. Figure 3 shows a clear correlation between $\rho_\star$, b_1, and b_2, which is expected as the transit duration is a geometrical measure of $\rho_\star$ for a circular orbit. There is also a correlation between b_1 and b_2, which demonstrates that relative inclinations are better measured than absolute inclinations. The correlation between $R_p/R_\star$ and b_1, and similarly with b_2, is due to stellar limb darkening.

Models 2 and 3 above allow us to explore how well we can measure eccentricity and limb darkening, and to understand potential biases in the measured planetary radii. Figure 4 shows the relative change in the measured value of $R_p/R_\star$ when comparing Model 2 against Model 1 (dots) and Model 3 versus Model 1 (stars) for each modeled planet. None of the model results differ by more than 1σ, except for KOI-438.02. In general, the uncertainty in $R_p/R_\star$ increases with model complexity. The fractional change in $R_p/R_\star$ between the three models is less than 5%, with most models showing differences smaller than 1.5%. Thus, the dominant source of error in the measurement of the planetary radius (R_p) is the error in the stellar radius.

The results of our transit model fits are presented in Table 8, in which, for completeness, we include the additional members of the four multiplanet systems as well (KOI-0172, 0438, 0812, and 2650). The values reported in the table correspond to the mode of the posterior distribution for each parameter based on our most simplistic model (Model 1) with a circular orbit and fixed quadratic limb-darkening coefficients. If future studies significantly increase the fidelity of the stellar parameters (e.g., through improvements coming from *Gaia* parallaxes), then a more complex photometric model may be warranted. In the case of KOI-438.02, Model 3 points toward a systematic increase in the measured scaled planetary radius, which is due to this model having a marginal preference for a noncircular orbit. This may indicate either a real eccentricity, or an error in the stellar parameters, for the following reason. The transit duration is proportional to the mean stellar density, and because we applied a prior on $\rho_\star$ informed by our spectroscopic work, any error in this quantity could lead to a mismatch in the expected transit duration for a circular orbit. The model accounts for the difference by making the orbit eccentric. Breaking this degeneracy requires either a more accurate measure of the fundamental stellar parameters or an independent determination of the eccentricity of the orbit.

Table 9 presents additional derived parameters from our fit, including the scaled semimajor axis $a/R_\star$, the fitted transit depth and total duration $\delta_{\rm tot}$, the duration of ingress/egress δ_{12} (interval between first and second contacts), the semimajor axis a and inclination angle i, the incident flux $S_{\rm eff}$ in units of the Earth's, and the equilibrium temperature of the planet $T_{\rm eq}$. The uncertainty in the latter accounts for a possible range of albedos between 0 and 0.5, as well as energy redistribution factors ranging from full redistribution to the planet being tidally locked. Our light-curve fits are illustrated in Figure 5. Because the modal values reported in Table 8 will generally not result in a best-fit light curve, to generate Figure 5, we chose to plot a transit model that is based on best-fit parameters.

The planetary radii listed in Table 8 assume that in each case the planet orbits the KOI. If instead the planet orbits a nearby companion, the true planetary size can be considerably larger because of the generally greater dilution of the signal caused by the brighter target star. The correction factor depends on the relative brightness ΔKp between the close neighbor and the target, and on the size of the companion (see also Ciardi et al. 2015; Furlan et al. 2017). Table 10 gives the relative brightness and angular separation of the close companions that are not excluded by centroid motion analysis or by `BLENDER`, along with the radius correction factors X_R and the R_p values

Table 8
Planet Properties Based on the Transit Models

KOI	R_p ($R_\oplus$)	Period (days)	T_0 (BJD-2,454,900)	$R_p/R_\star$	b	$\rho_\star$ ($e = 0$) (g cm^{-3})	S/N
KOI-0172.01	2.36	13.722353	70.84153	0.02211	0.0094	0.913	97.6
	+0.30/−0.21	± 0.000016	± 0.00080	+0.00015/−0.00015	+0.1846/−0.0094	+0.021/−0.049	
KOI-0172.02	1.79	242.4659	83.8693	0.01669	0.28	0.913	21.4
	+0.22/−0.18	± 0.0027	± 0.0080	+0.00033/−0.00049	+0.10/−0.13	+0.021/−0.049	
KOI-0438.01	1.73	5.9311924	107.79717	0.03065	0.0086	4.73	76.6
	+0.28/−0.27	± 0.0000042	± 0.00059	+0.00020/−0.00023	+0.1853/−0.0086	+0.19/−0.27	
KOI-0438.02	1.97	52.661560	116.5188	0.03431	0.776	4.73	31.6
	+0.19/−0.48	± 0.000111	± 0.0018	+0.00043/−0.00064	+0.012/−0.015	+0.19/−0.27	
KOI-0463.01	1.47	18.4776440	118.26823	0.04902	0.506	18.8	71.4
	+0.16/−0.22	± 0.0000111	± 0.00052	+0.00059/−0.00092	+0.062/−0.216	+5.9/−2.8	
KOI-0812.01	2.169	3.3402178	104.97911	0.03990	0.160	4.82	69.3
	+0.078/−0.124	± 0.0000021	± 0.00058	+0.00029/−0.00029	+0.057/−0.129	+0.14/−0.23	
KOI-0812.02	2.024	20.060390	80.4646	0.03763	0.358	4.82	34.7
	+0.098/−0.100	± 0.000049	± 0.0020	+0.00059/−0.00059	+0.063/−0.053	+0.14/−0.23	
KOI-0812.03	2.007	46.18406	98.2376	0.03725	0.0041	4.82	27.7
	+0.098/−0.100	± 0.00027	± 0.0039	+0.00067/−0.00065	+0.0804/−0.0041	+0.14/−0.23	
KOI-0812.04	1.201	7.825046	69.5503	0.02239	0.390	4.82	14.8
	+0.067/−0.067	± 0.000030	± 0.0038	+0.00069/−0.00069	+0.072/−0.101	+0.14/−0.23	
KOI-0854.01	2.76	56.05623	134.1648	0.0503	0.018	5.55	26.5
	+0.15/−0.22	± 0.00019	± 0.0026	+0.0027/−0.0027	+0.105/−0.018	+0.28/−0.24	
KOI-2418.01	1.34	86.82974	122.2617	0.02708	0.0068	6.13	16.7
	+0.09/−0.14	± 0.00080	± 0.0052	+0.00085/−0.00085	+0.1353/−0.0068	+0.61/−0.53	
KOI-2626.01	1.60	38.09722	73.0045	0.0387	0.011	9.90	16.2
	+0.18/−0.18	± 0.00021	± 0.0047	+0.0016/−0.0018	+0.233/−0.011	+0.88/−1.34	
KOI-2650.01	1.336	34.98956	77.2154	0.02259	0.047	4.83	12.8
	+0.072/−0.072	± 0.00022	± 0.0063	+0.00060/−0.00106	+0.093/−0.047	+0.16/−0.36	
KOI-2650.02	1.186	7.054259	69.1958	0.01980	0.688	4.83	11.7
	+0.061/−0.087	± 0.000027	± 0.0037	+0.00093/−0.00092	+0.028/−0.066	+0.16/−0.36	
KOI-3010.01	2.15	60.86628	112.2847	0.0351	0.423	4.63	16.4
	+0.12/−0.17	± 0.00049	± 0.0069	+0.0013/−0.0019	+0.060/−0.194	+0.55/−0.21	
KOI-3282.01	1.93	49.27668	90.0267	0.0350	0.514	5.67	24.2
	+0.19/−0.20	± 0.00068	± 0.0117	+0.0014/−0.0024	+0.078/−0.258	+1.42/−0.72	
KOI-3497.01	0.80	20.359722	67.2911	0.01895	0.637	10.2	35.5
	+0.13/−0.13	± 0.000076	± 0.0025	+0.00087/−0.00101	+0.075/−0.265	+6.1/−2.1	
KOI-4036.01	1.790	168.8116	144.4420	0.02291	0.584	2.90	28.3
	+0.079/−0.119	± 0.0020	± 0.0075	+0.00088/−0.00088	+0.051/−0.072	+0.22/−0.22	
KOI-4054.01	2.08	169.1335	134.8148	0.02316	0.293	2.24	27.4
	+0.11/−0.14	± 0.0018	± 0.0096	+0.00076/−0.00076	+0.075/−0.208	+0.16/−0.21	
KOI-4356.01	2.91	174.5085	134.482	0.0381	0.46	3.03	18.2
	+0.17/−0.25	± 0.0029	± 0.014	+0.0018/−0.0028	+0.13/−0.17	+0.22/−0.22	
KOI-4450.01	2.23	196.4356	106.704	0.0225	0.48	1.67	16.2
	+0.31/−0.23	± 0.0073	± 0.037	+0.0017/−0.0017	+0.16/−0.27	+0.24/−0.36	
KOI-4550.01	2.17	140.2524	108.134	0.0286	0.52	3.08	8.9
	+0.16/−0.23	± 0.0030	± 0.017	+0.0019/−0.0027	+0.13/−0.17	+0.19/−0.27	
KOI-5236.01	2.07	550.864	240.691	0.01801	0.52	1.00	21.8
	+0.32/−0.20	± 0.014	± 0.017	+0.00076/−0.00075	+0.10/−0.26	+0.41/−0.12	
KOI-5856.01	1.60	259.365	98.600	0.0184	0.014	0.56	13.9
	+0.32/−0.19	± 0.014	± 0.042	+0.0011/−0.0011	+0.272/−0.014	+0.10/−0.17	

Note. Properties of the KOIs based on our transit light-curve modeling via MCMC. Uncertainties representing credible 68.3% confidence intervals are given below each parameter (asymmetric error bars are reported when warranted). The main model parameters are the period, T_0, $R_p/R_\star$, b, and $\rho_\star$. The photometric model assumes a circular orbit. The planetary radius, R_p, is the product of $R_p/R_\star$ and the stellar radius $R_\star$ from Table 6. The S/N was computed using Equation (5) of Rowe et al. (2015).

that apply if the planet orbits the companion. These planetary radii are seen to be typically ∼50% larger than those in Table 8. In most cases, these larger sizes would compromise potential habitability because they would imply that the planets are more likely gaseous than rocky.

8. Habitability

The MCMC analysis of the *Kepler* light curves together with the stellar properties described earlier provide probability distributions for the planetary and stellar parameters. Here, we have combined these distributions with calculations for the HZ

Table 9
Derived Planet Properties Based on Our Transit Models

KOI	$a/R_\star$	Depth (ppm)	δ_{tot} (hr)	δ_{12} (hr)	a (au)	i (degrees)	S_{eff} ($S_\oplus$)	T_{eq} (K)
KOI-0172.01	20.84	591.8	5.126	0.1109	0.1091	89.975	76	867
	+0.12/−0.50	± 6.0	± 0.024	± 0.0052	+0.0015/−0.0021	+0.0015/−0.459	+22/−16	+71/−90
KOI-0172.02	141.39	333	13.10	0.2216	0.740	89.901	1.64	325
	+0.84/−3.37	± 14	± 0.25	± 0.0145	+0.011/−0.013	+0.011/−0.052	+0.48/−0.34	+35/−27
KOI-0438.01	20.69	1035.1	2.250	0.0672	0.0526	89.88	19.0	614
	+0.21/−0.49	± 11.6	± 0.018	± 0.0026	+0.0022/−0.0031	+0.0022/−0.37	+8.6/−11.3	+73/−107
KOI-0438.02	88.72	1088	3.136	0.247	0.2254	89.495	1.03	286
	+0.90/−2.09	± 27	± 0.045	± 0.013	+0.0092/−0.0139	+0.0092/−0.032	+0.47/−0.61	+46/−41
KOI-0463.01	69.1	2779	1.879	0.0864	0.0899	89.606	1.18	298
	+7.9/−2.3	± 36	± 0.022	± 0.0151	+0.0031/−0.0062	+0.0031/−0.094	+0.22/−0.28	+22/−32
KOI-0812.01	14.15	1844	1.8672	0.07176	0.03482	89.47	44.0	731
	+0.13/−0.23	± 25	± 0.0122	± 0.00201	+0.00042/−0.00056	+0.00042/−0.33	+6.5/−5.2	+67/−52
KOI-0812.02	46.76	1620	3.197	0.1334	0.1150	89.576	4.03	401
	+0.42/−0.76	± 46	± 0.054	± 0.0058	+0.0014/−0.0018	+0.0014/−0.066	+0.60/−0.48	+38/−27
KOI-0812.03	81.52	1619	4.484	0.1630	0.2012	89.9971	1.33	306
	+0.73/−1.33	± 56	± 0.060	± 0.0036	+0.0022/−0.0034	+0.0022/−0.0524	+0.20/−0.16	+24/−25
KOI-0812.04	24.96	570	2.289	0.0578	0.06141	89.16	14.2	555
	+0.22/−0.41	± 33	± 0.071	± 0.0037	+0.00074/−0.00099	+0.00074/−0.19	+2.1/−1.7	+43/−46
KOI-0854.01	97.3	1851	4.574	0.221	0.2320	89.990	0.729	265
	+1.9/−1.1	± 62	± 0.067	± 0.013	+0.0037/−0.0022	+0.0037/−0.060	+0.091/−0.066	+21/−21
KOI-2418.01	134.6	857	4.97	0.1335	0.3006	89.9971	0.296	212
	+5.2/−2.9	± 51	± 0.14	± 0.0060	+0.0069/−0.0091	+0.0069/−0.0533	+0.073/−0.037	+19/−17
KOI-2626.01	91.0	977	3.24	0.1232	0.1654	89.9927	0.81	268
	+3.3/−3.5	± 63	± 0.12	± 0.0091	+0.0042/−0.0075	+0.0042/−0.1432	+0.16/−0.13	+27/−20
KOI-2650.01	67.77	593	4.018	0.0896	0.1743	89.960	2.11	341
	+0.68/−1.84	± 44	± 0.078	± 0.0038	+0.0023/−0.0023	+0.0023/−0.077	+0.19/−0.25	+27/−27
KOI-2650.02	23.30	423	1.765	0.0628	0.05993	88.36	17.8	576
	+0.23/−0.63	± 33	± 0.087	± 0.0060	+0.00079/−0.00078	+0.00079/−0.14	+1.6/−2.1	+55/−36
KOI-3010.01	96.9	882	4.53	0.175	0.2543	89.750	1.06	290
	+3.7/−1.5	± 58	± 0.17	± 0.016	+0.0043/−0.0038	+0.0043/−0.052	+0.11/−0.15	+21/−24
KOI-3282.01	89.3	1377	3.79	0.138	0.2149	89.693	1.16	298
	+7.8/−3.2	± 135	± 0.21	± 0.023	+0.0055/−0.0054	+0.0055/−0.089	+0.29/−0.31	+28/−28
KOI-3497.01	60.1	317	2.094	0.0387	0.1097	89.45	1.60	322
	+11.4/−2.9	± 19	± 0.094	± 0.0128	+0.0045/−0.0079	+0.0045/−0.14	+0.44/−0.51	+27/−40
KOI-4036.01	163.2	601	6.61	0.219	0.5421	89.797	0.82	269
	+4.2/−4.1	± 38	± 0.26	± 0.020	+0.0069/−0.0088	+0.0069/−0.022	+0.13/−0.10	+25/−20
KOI-4054.01	149.5	661	8.57	0.200	0.5715	89.889	1.42	309
	+4.2/−4.0	± 40	± 0.21	± 0.015	+0.0069/−0.0103	+0.0069/−0.036	+0.19/−0.23	+29/−23
KOI-4356.01	169.1	1759	7.64	0.320	0.5460	89.847	0.715	260
	+4.5/−3.7	± 173	± 0.44	± 0.043	+0.0112/−0.0048	+0.0112/−0.050	+0.113/−0.089	+24/−19
KOI-4450.01	151.8	605	9.40	0.225	0.6421	89.814	1.56	324
	+6.9/−11.1	± 80	± 0.81	± 0.046	+0.0108/−0.0089	+0.0108/−0.065	+0.36/−0.31	+28/−32
KOI-4550.01	146.7	665	6.60	0.236	0.4706	89.788	0.98	284
	+4.2/−3.2	± 80	± 0.52	± 0.038	+0.0098/−0.0041	+0.0098/−0.053	+0.18/−0.10	+25/−21
KOI-5236.01	276.4	373	14.76	0.273	1.297	89.889	0.77	273
	+9.5/−31.2	± 27	± 0.51	± 0.056	+0.014/−0.020	+0.014/−0.032	+0.21/−0.16	+23/−27
KOI-5856.01	127.3	395	15.73	0.291	0.745	89.9954	1.17	304
	+4.9/−16.1	± 45	± 1.08	± 0.046	+0.021/−0.020	+0.0021/−0.0844	+0.58/−0.28	+39/−31

Note. Additional derived properties of our KOIs based on our transit light-curve modeling via MCMC (see Table 8). Uncertainties representing credible 68.3% confidence intervals are given below each parameter (asymmetric error bars are given when warranted). The values of $a/R_\star$ and the incident flux (S_{eff}) were calculated using Equation (2) and Equation (4) from Rowe et al. (2015). δ_{tot} is the total depth of the transit model evaluated at time T_0 and δ_{12} is the duration of ingress (first to second contact). The values of δ_{tot} and δ_{12} were derived from Equation (3) and Equation (2) of Seager and Mallén-Ornelas (2003).

in order to quantify the probability that the planets lie in the HZ, and we assume for these estimates that the planets orbit the target. The boundaries of the HZ were calculated using the empirically derived relations presented by Kopparapu et al. (2013, 2014). We used both the "conservative" (CHZ) and "optimistic" (OHZ) boundaries for the HZ detailed by Kane et al. (2016), the locations of which are determined based upon assumptions regarding how long Venus and Mars may have been able to retain liquid water on their surfaces. The stellar fluxes, S_{eff}, at each HZ boundary were determined from a polynomial relationship involving the effective temperature T_{eff}. The HZ boundaries were then calculated from

$$d = (L_\star/S_{eff})^{1/2} \text{ au}, \quad (1)$$

where $L_\star$ is the luminosity of the star in solar units.

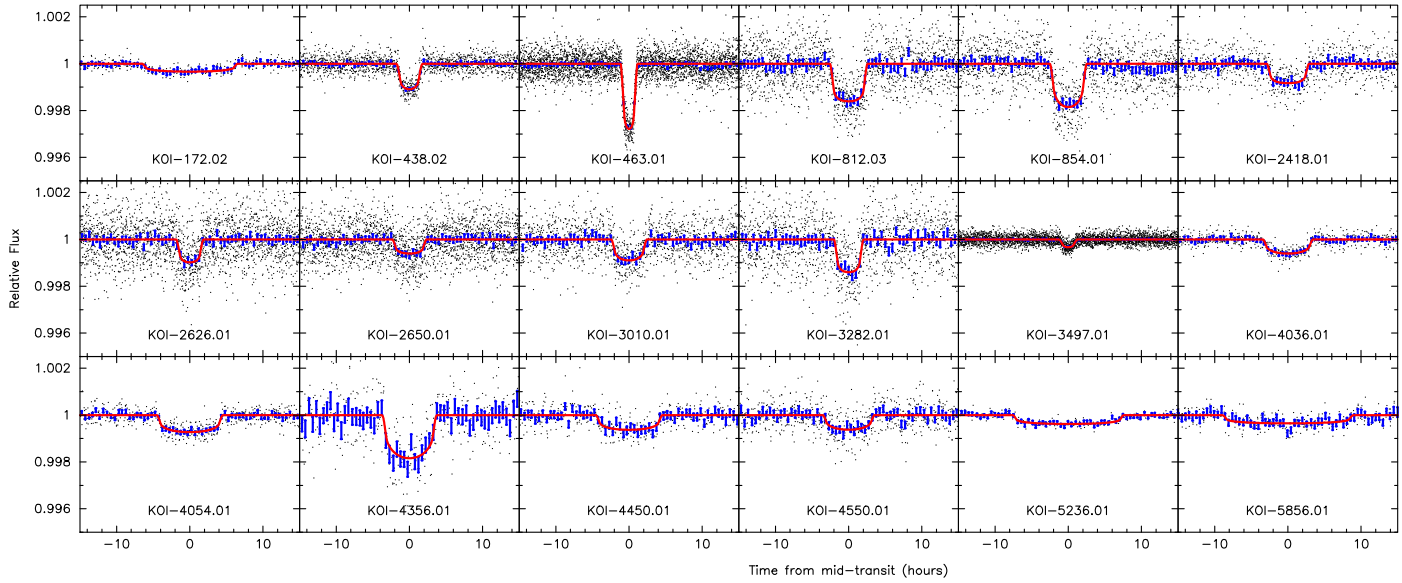

Figure 5. Light-curve fits (red lines) and *Kepler* observations within 15 hr of the center-of-transit time for our 18 KOIs. The observations shown as black dots are a combination of short- and long-cadence data. Blue symbols represent data averaged in 30 minute bins, with 1σ error bars computed from the standard deviation.

Table 10
Planetary Radii Corrected for Dilution, for Stars in Which the Planet Transits a Fainter Nearby Companion Rather than the Target

Name	ρ ($''$)	ΔKp (mag)	$M_{\rm comp}$ ($M_\odot$)	$R_{\rm comp}$ ($R_\odot$)	X_R	R_p comp. ($R_\oplus$)
KOI-0854.01	0.016	0.39	0.49	0.46	1.44	3.96
KOI-2418.01	0.108	3.32	0.12	0.14	1.48	1.98
KOI-2626.01	0.164	1.46	0.24	0.24	1.66	2.66
KOI-2626.01	0.206	0.62	0.33	0.32	1.49	2.38
KOI-3010.01	0.334	0.43	0.55	0.52	1.46	3.14
KOI-3497.01	0.795	1.31	0.25	0.25	1.35	1.08
KOI-4550.01	1.045	0.89	0.63	0.61	1.61	3.48

Note. The columns list the angular separation of the companion and the estimated brightness difference relative to the target in the *Kp* band, the estimated mass and radius of the companion star, the correction factor X_R for the planetary radius, and the corrected radius if the planet transits the companion.

Shown in Figure 6 are representations of the joint posterior distributions for the planetary radius and the incident flux for each of the 18 KOIs analyzed in this work. In each panel, we used the same range of planetary radii on the vertical axes, and the horizontal axes are scaled so that the OHZ boundaries are aligned to facilitate the comparison. The inner and outer CHZ and OHZ boundaries are indicated by the vertical dotted lines, and a horizontal dashed line shows the location where $R_p = 2.0\,R_\oplus$, for reference. The methodology of Kane et al. (2016) defines a category of HZ candidates that lie inside the OHZ and have radii less than $2\,R_\oplus$. The rationale behind this radius boundary is that in many cases (depending on composition, incident flux, etc.), the transition between a rocky and a gaseous planet occurs somewhere between 1.5 and $2.0\,R_\oplus$ (Weiss & Marcy 2014; Rogers 2015; Wolfgang & Lopez 2015; Fulton et al. 2017). Given the uncertainties on the planetary and stellar properties, Kane et al. (2016) chose an upper radius limit of $2\,R_\oplus$ to define their list of likely terrestrial candidates within the OHZ (see their Table 2).

Using a procedure similar to that of Torres et al. (2015), we further calculated the probability that each candidate falls within the region defined by the OHZ and the $R_p \leqslant 2.0\,R_\oplus$ boundaries. This was done for each type of boundary by determining the number of posterior realizations that lie within the corresponding region. The results of these calculations are presented in Table 11. They show that 15 of the 18 candidates have a greater than 50% chance of lying within the OHZ, 10 of the candidates meet the $R_p \leqslant 2.0\,R_\oplus$ criterion, and 7 meet both criteria.

9. Discussion

Of the 18 planet candidates on our target list, we validated 15 at a confidence level of 99.73% or higher (3σ). The other three (KOI-4054.01, KOI-4450.01, and KOI-5236.01) are currently validated at slightly lower levels of 99.5%–99.6% (2.8σ–2.9σ), which could be improved with further spectroscopic or deep imaging observations to help rule out additional false positives. The 18 objects span a range of planetary radii from about 0.80 to $2.9\,R_\oplus$. Seven of them (KOI-0438.02, 0463.01, 2418.01, 2626.01, 3282.01, 4036.01, and 5856.01) have the best chance (>50%) of being in the optimistic HZ and at the same time being smaller than $2\,R_\oplus$. As such, they are valuable for studies of the rate of occurrence of small planets in the HZ of their host stars, one of the primary science goals of the *Kepler* Mission. All but one of these six orbit an M dwarf, and their orbital periods range from 18 to 169 days. Among them, we note that KOI-0438.02 was not included in the catalog of small HZ planets by Kane et al. (2016) because the stellar radius and pipeline transit modeling parameters adopted in that work (DR25; Thompson et al. 2017) placed the planet just above the $2\,R_\oplus$ cutoff they used, whereas we now measure a size just below it.

The 18 KOIs studied in this work with BLENDER have been previously subjected to a similar statistical validation exercise using the VESPA procedure (Morton et al. 2016),[22] with the

[22] VESPA is an open-source code available to the community; the more computer-intensive BLENDER code was custom-designed to run on the Pleiades supercomputer at the NASA Ames Research Center (CA).

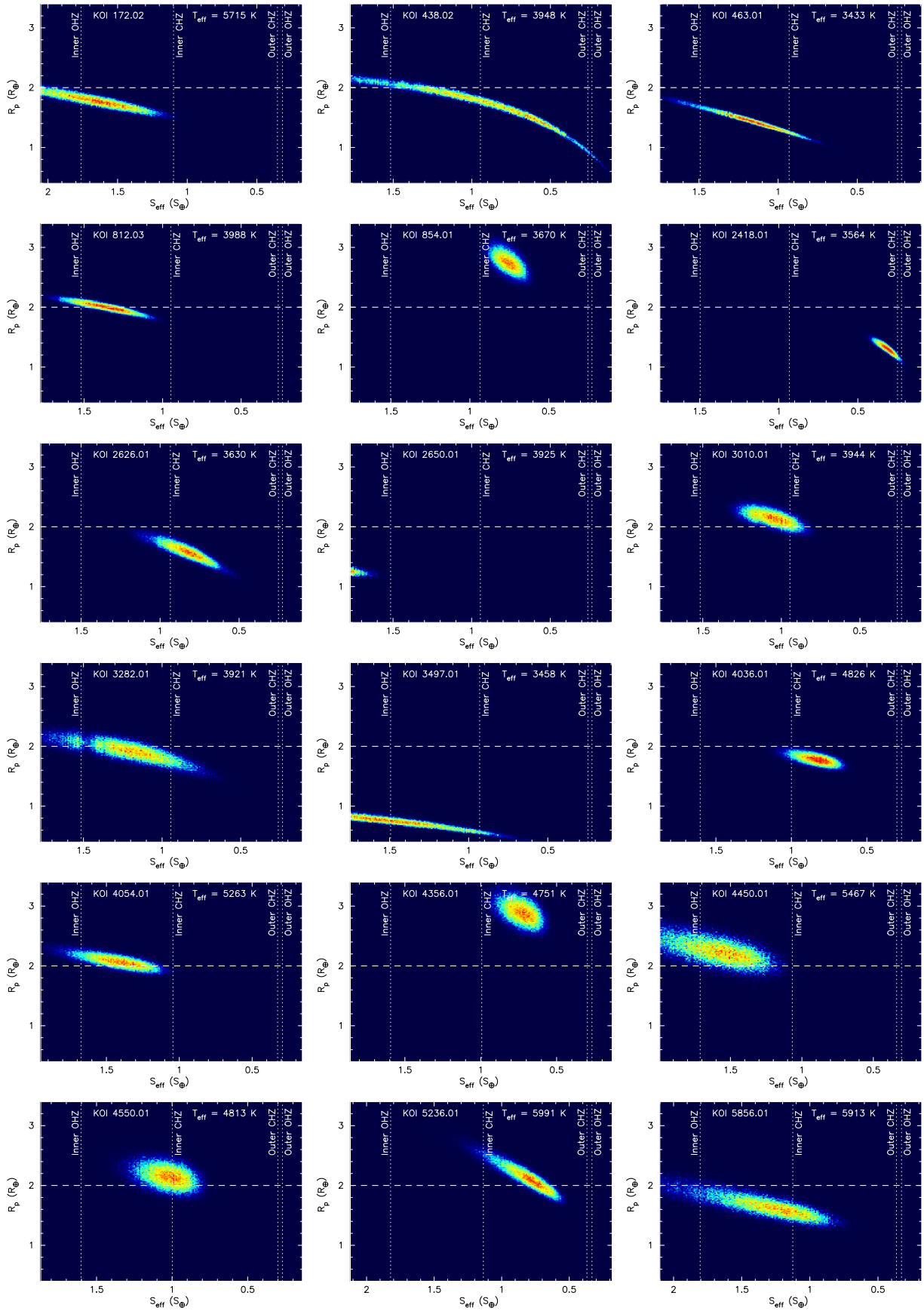

Figure 6. Heat maps of the joint posterior distributions for the planetary radii R_p and stellar fluxes $S_{\rm eff}$ for each of our KOIs. They are shown in units of Earth radii and the incident flux received by the Earth from the Sun, respectively. The vertical dotted lines show the locations of the conservative HZ (CHZ) and optimistic HZ (OHZ) boundaries, and the horizontal dashed line marks a planetary radius of 2 $R_\oplus$, for reference.

Table 11
Probability of the KOIs Meeting the OHZ and $R_p \leqslant 2\,R_\oplus$ Criteria

Name	Within OHZ (%)	$R_p \leqslant 2\,R_\oplus$ (%)
KOI-0172.02	46.1	74.5
KOI-0438.02	73.2	65.4
KOI-0463.01	85.0	99.8
KOI-0812.03	79.5	46.0
KOI-0854.01	100.0	0.0
KOI-2418.01	97.4	100.0
KOI-2626.01	100.0	98.7
KOI-2650.01	0.1	100.0
KOI-3010.01	100.0	14.1
KOI-3282.01	79.9	62.4
KOI-3497.01	38.7	100.0
KOI-4036.01	100.0	97.8
KOI-4054.01	83.6	22.9
KOI-4356.01	100.0	0.0
KOI-4450.01	53.7	9.2
KOI-4550.01	99.9	19.2
KOI-5236.01	99.9	23.3
KOI-5856.01	72.7	79.3

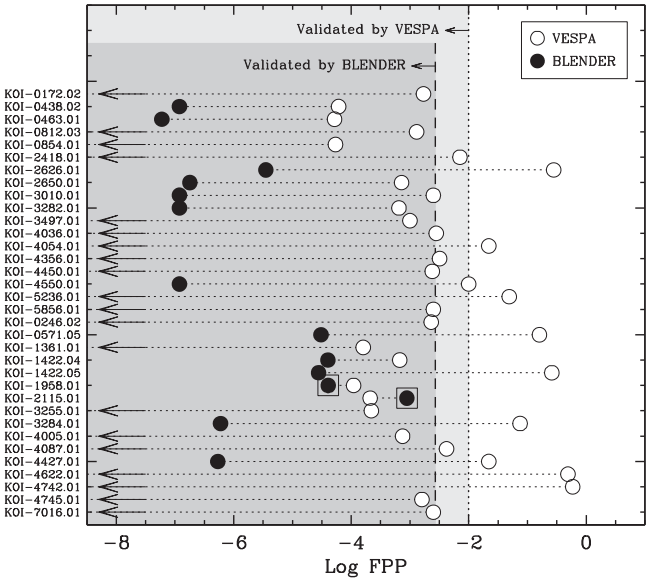

Figure 7. Comparison between false-positive probabilities from BLENDER (excluding HTP and BP scenarios) and VESPA for 34 KOIs subject to validation by both methods, as labeled on the left. Those from the present work are indicated in bold at the top. Arrows represent upper limits from BLENDER, and the two values marked with squares (KOI-1958.01 and KOI-2115.01; Meibom et al. 2013) correspond to special cases in which the BLENDER validations used more conservative assumptions than usual for the planet priors (see text). For candidates to be declared validated with VESPA, they are required to be to the left of the dotted line (FPP $\leqslant$ 0.01; light gray area), whereas validated planets from BLENDER are those to the left of the dashed line (FPP $\leqslant$ 0.0027; darker gray area).

result that all but three of them (KOI-2626.01, KOI-4054.01, and KOI-5236.01) were considered validated with that algorithm at the 99% or higher confidence level. Given that the two methodologies are completely independent, it is of interest to compare the false-positive probabilities (FPPs) returned by each approach. As pointed out earlier, one of the key conceptual differences between BLENDER and VESPA is that VESPA does not consider as false positives configurations that involve a planet transiting a star different from the target along the same line of sight. These correspond to the scenarios we referred to here as BP and HTP, and we argued that for applications such as ours, where the size of the planet is important, they should be included in calculating the FPP. To place the FPPs from both methods on the same footing for this comparison, we recomputed those from BLENDER as FPP = BEB/(PL + BEB), leaving out the blend frequencies from the HTP and BP scenarios. The top portion of Figure 7 shows the FPPs from BLENDER and VESPA for our 18 targets (names in boldface). An additional 16 candidates from the literature have been examined in recent years both with VESPA and with a version of BLENDER essentially the same as that used here (Barclay et al. 2013; Meibom et al. 2013; Jenkins et al. 2015; Torres et al. 2015), and we include them in the comparison as well. Arrows indicate upper limits from BLENDER for cases in which blends with background/foreground eclipsing binaries are virtually all excluded simply from the shape of the transits.

Overall, the more detailed treatment given to each candidate in BLENDER, and perhaps the more elaborate assumptions, results in validations that are typically stronger than those from VESPA, with FPP values that are an order of magnitude or more smaller.[23] Under the conditions of this comparison (i.e., excluding HTP and BP scenarios), all 34 candidates are validated with BLENDER at the 99.73% (3σ) confidence level or higher ($\log \mathrm{FPP} < -2.57$; dashed line), in the sense of indicating the probable presence of a planet somewhere in the system (not necessarily orbiting the target). The success rate for VESPA (at the 99% confidence level) for the same sample is about 70%. On the other hand, by being computationally simpler, VESPA is designed to allow the quick and automatic application to large numbers of *Kepler* candidates, something that is not practical with BLENDER.

The statistical validation of small candidate transiting planets in or near the HZ is especially challenging for any method because the signals are small and the periods tend to be long, resulting in fewer transits over the duration of the observations. Both of these contribute to lower S/Ns, which results in a less well-defined shape for the transit with which to rule out blends. These types of candidates benefit the most from close attention to the circumstances of each one and the use of every available piece of information from follow-up observations that can help exclude scenarios that could mimic transits. Still, the possibility always remains that further scrutiny may reveal a "validated" planet to be a false positive of one kind or another. Several examples of such "unvalidated" or disproven transiting planets have appeared in the recent literature. Three cases from the *K2* Mission (K2-78 b, K2-82 b, and K2-92 b) that had been validated as planets with radii in the 1.4–2.6 $R_\oplus$ range (Crossfield et al. 2016) turned out to be background eclipsing binaries, as shown by Cabrera et al. (2017). In two of the cases, the eclipsing binaries were outside the area covered by the high-resolution imaging observations and had been overlooked, or produced a clear signature in the flux centroids that had not been examined, and in the other case there were visible

[23] There are two exceptions marked in Figure 7 with squares, for which the BLENDER and VESPA FPP values are most similar. They correspond to KOI-1958.01 and KOI-2115.01 (also Kepler-66 b and Kepler-67 b; Meibom et al. 2013), which are the first two transiting planets discovered in an open cluster (NGC 6811). The BLENDER validations for these candidates adopted much more conservative assumptions than usual about the planet prior because of the poorly known planet occurrence rate in clusters, and this resulted in significantly higher FPP values than would have been obtained if the host stars had been in the field.

secondary eclipses that had been missed. For three other validated *K2* planets (K2-51 b, K2-67 b, and K2-76 b), the transit signals were found to be due to companions that are low-mass stars rather than planets (Shporer et al. 2017). In two of them, the host stars had poorly estimated properties, and in the other, the size of the stellar companion is small enough that it is difficult to distinguish it from a giant planet. These examples serve as a stark reminder not only of the probabilistic nature of the validations, but also of the critical importance of careful attention to detail in the use of stellar properties and follow-up constraints.

We thank the anonymous referee for helpful comments on the original manuscript. This paper includes data collected by the *Kepler* spacecraft. Funding for the *Kepler* Mission is provided by NASA's Science Mission Directorate. Resources supporting this work were provided by the NASA High-End Computing (HEC) Program through the NASA Advanced Supercomputing (NAS) Division at Ames Research Center. The research has also made use of NASA's Astrophysics Data System (ADS) and of data products from the Mikulski Archive for Space Telescopes (MAST). Some of the data presented herein were obtained at the W. M. Keck Observatory, which is operated as a scientific partnership among the California Institute of Technology, the University of California, and NASA. We extend special thanks to those of Hawaiian ancestry on whose sacred mountain of Maunakea we are privileged to be guests. G.T. acknowledges partial support for this work from NASA grant NNX14AB83G (*Kepler* Participating Scientist Program) and Cooperative Agreement NNX13AB58A with the Smithsonian Astrophysical Observatory (PI: D.W.L.). This research was enabled in part by support provided by Calcul Québec (http://www.calculquebec.ca) and Compute Canada (http://www.computecanada.ca).

ORCID iDs

Guillermo Torres https://orcid.org/0000-0002-5286-0251
Stephen R. Kane https://orcid.org/0000-0002-7084-0529
Jason F. Rowe https://orcid.org/0000-0002-5904-1865
Thomas Barclay https://orcid.org/0000-0001-7139-2724
Lars A. Buchhave https://orcid.org/0000-0003-1605-5666
Justin R. Crepp https://orcid.org/0000-0003-0800-0593
Mark E. Everett https://orcid.org/0000-0002-0885-7215
Elliott P. Horch https://orcid.org/0000-0003-2159-1463
Andrew W. Howard https://orcid.org/0000-0001-8638-0320
Steve B. Howell https://orcid.org/0000-0002-2532-2853
Howard T. Isaacson https://orcid.org/0000-0002-0531-1073
Jon M. Jenkins https://orcid.org/0000-0002-4715-9460
David W. Latham https://orcid.org/0000-0001-9911-7388
Erik A. Petigura https://orcid.org/0000-0003-0967-2893

References

Baranec, C., Ziegler, C., Law, N. M., et al. 2016, AJ, 152, 18
Barclay, T., Burke, C. J., Howell, S. B., et al. 2013, ApJ, 768, 101
Borucki, W. J. 2016, RPPh, 79, 036901
Borucki, W. J., Agol, E., Fressin, F., et al. 2013, Sci, 340, 587
Brown, T. M., Latham, D. W., Everett, M. E., & Esquerdo, G. A. 2011, AJ, 142, 112
Bryson, S. T., Jenkins, J. M., Gilliland, R. L., et al. 2013, PASP, 125, 889
Buchhave, L. A., Latham, D. W., Anders, J., et al. 2012, Natur, 486, 375
Burke, C. J., Christiansen, J. L., Mullally, F., et al. 2015, ApJ, 809, 8
Cabrera, J., Barros, S. C. C., Armstrong, D., et al. 2017, A&A, 606, A75
Ciardi, D. R., Beichman, C. A., Horch, E. P., & Howell, S. B. 2015, ApJ, 805, 16
Claret, A., & Bloemen, S. 2011, A&A, 529, A75
Coughlin, J. L., Mullally, F., Thompson, S. E., et al. 2016, ApJS, 224, 12
Crossfield, I. J. M., Ciardi, D. R., Petigura, E. A., et al. 2016, ApJS, 226, 7
Cutri, R. M., Skrutskie, M. F., van Dyk, S., et al. 2003, The 2MASS All-Sky Catalog of Point Sources, Univ. of Massachusetts and Infrared Processing and Analysis Center (IPAC/California Institute of Technology), yCat, 2246, 0
Dotter, A., Chaboyer, B., Darko, J., et al. 2008, ApJS, 178, 89
Dressing, C. D., & Charbonneau, D. 2013, ApJ, 767, 95
Dressing, C. D., & Charbonneau, D. 2015, ApJ, 807, 45
Endl, M., & Cochran, W. D. 2016, PASP, 128, 094502
Epstein, C. R., & Pinsonneault, M. H. 2014, ApJ, 780, 159
Everett, M. E., Howell, S. B., & Kinemuchi, K. 2012, PASP, 124, 316
Everett, M. E., Howell, S. B., Silva, D. R., & Szkody, P. 2013, ApJ, 771, 107
Ford, E. B. 2005, AJ, 129, 1706
Foreman-Mackey, D. 2016, corner.py on GitHub, https://github.com/dfm/corner.py
Fressin, F., Torres, G., Charbonneau, D., et al. 2013, ApJ, 766, 81
Fressin, F., Torres, G., Rowe, J. F., et al. 2012, Natur, 482, 195
Fulton, B. J., Petigura, E. A., Howard, A. W., et al. 2017, arXiv:1703.10375
Fűrész, G. 2008, PhD thesis, Univ. Szeged
Furlan, E., Ciardi, D. R., Everett, M. E., et al. 2017, AJ, 153, 71
Gilliland, R. L., Cartier, K. M. S., Adams, E. R., et al. 2015, AJ, 149, 24
Hayward, T. L., Brandl, B., Pirger, B., et al. 2001, PASP, 113, 105
Henden, A. A., Levine, S. E., Terrell, D., Smith, T. C., & Welch, D. 2012, JAVSO, 40, 430
Hirsch, L. A., Ciardi, D. R., Howard, A. W., et al. 2017, AJ, 153, 117
Horch, E. P., Falta, D., Anderson, L. M., et al. 2010, AJ, 139, 205
Horch, E. P., Howell, S. B., Everett, M. E., & Ciardi, D. R. 2014, ApJ, 795, 60
Horch, E. P., Veillette, D. R., Baena Gallé, R., et al. 2009, AJ, 137, 5057
Huber, D., Silva Aguirre, V., Matthews, J. M., et al. 2014, ApJS, 211, 2
Jenkins, J. M., Caldwell, D. A., & Borucki, W. J. 2002, ApJ, 564, 495
Jenkins, J. M., Twicken, J. D., Batalha, N. M., et al. 2015, AJ, 150, 56
Kane, S. R., Hill, M. L., Kasting, J. F., et al. 2016, ApJ, 830, 1
Kipping, D. M. 2013, MNRAS, 435, 2152
Kipping, D. M., Torres, G., Buchhave, L. A., et al. 2014, ApJ, 795, 25
Kipping, D. M., Torres, G., Henze, C., et al. 2016, ApJ, 820, 112
Kolbl, R., Marcy, G. W., Isaacson, H., & Howard, A. W. 2015, AJ, 149, 18
Kopparapu, R. K. 2013, ApJL, 767, L8
Kopparapu, R. K., Ramirez, R., Kasting, J. F., et al. 2013, ApJ, 765, 131
Kopparapu, R. K., Ramirez, R. M., SchottelKotte, J., et al. 2014, ApJ, 787, 29
Kraus, A. L., Ireland, M. J., Huber, D., Mann, A. W., & Dupuy, T. J. 2016, AJ, 152, 8
Lissauer, J. J., Marcy, G. W., Bryson, S. T., et al. 2014, ApJ, 784, 44
Mandel, K., & Agol, E. 2002, ApJL, 580, L171
Mann, A. W., Gaidos, E., & Ansdell, M. 2013a, ApJ, 779, 188
Mann, A. W., Gaidos, E., Kraus, A., & Hilton, E. J. 2013b, ApJ, 770, 43
Mathur, S., Huber, D., Batalha, N. M., et al. 2017, ApJS, 229, 30
McQuillan, A., Aigrain, S., & Mazeh, T. 2013a, MNRAS, 432, 1203
McQuillan, A., Mazeh, T., & Aigrain, S. 2013b, ApJL, 775, L11
Meibom, S., Torres, G., Fressin, F., et al. 2013, Natur, 499, 55
More, J., Garbow, B., & Hillstrom, K. 1980, Argoone National Laboratory Report ANL-80-74
Morton, T. D., Bryson, S. T., Coughlin, J. L., et al. 2016, ApJ, 822, 86
Muirhead, P. S., Becker, J., Feiden, G. A., et al. 2014, ApJS, 213, 5
Muirhead, P. S., Hamren, K., Schlawin, E., et al. 2012, ApJ, 750, 37
Mulders, G. D., Pascucci, I., & Apai, D. 2015, ApJ, 798, 112
Newton, E. R., Charbonneau, D., Irwin, J., & Mann, A. W. 2015, ApJ, 800, 85
Nielsen, M. B., Gizon, L., Schunker, H., & Karoff, C. 2013, A&A, 557, L10
Reinhold, T., Reiners, A., & Basri, G. 2013, A&A, 560, A4
Rogers, L. A. 2015, ApJ, 801, 41
Rojas-Ayala, B., Covey, K. R., Muirhead, P. S., & Lloyd, J. P. 2012, ApJ, 748, 93
Rowe, J. F. 2016, Kepler: Kepler Transit Model Codebase Release, Zenodo, doi:10.5281/zenodo.60297
Rowe, J. F., Bryson, S. T., Marcy, G. W., et al. 2014, ApJ, 784, 45
Rowe, J. F., Coughlin, J. L., Antoci, V., et al. 2015, ApJS, 217, 16
Seager, S., & Mallén-Ornelas, G. 2003, ApJ, 585, 1038
Shporer, A., Zhou, G., Venderburg, A., et al. 2017, ApJ, 847, 18
Stumpe, M. C., Smith, J. C., Catanzarite, J. H., et al. 2014, PASP, 126, 100
Terrien, R. C., Mahadevan, S., Bender, C. F., et al. 2012, ApJL, 747, L38
Thompson, S. E., Coughlin, J. L., Hoffman, K., et al. 2017, ApJS, submitted, arXiv:1710.06758
Torres, G., Fressin, F., Batalha, N. M., et al. 2011, ApJ, 727, 24

Torres, G., Kipping, D. M., Fressin, F., et al. 2015, ApJ, 800, 99
Torres, G., Konacki, M., Sasselov, D. D., & Jha, S. 2004, ApJ, 614, 979
Tull, R. G., MacQueen, P. J., Sneden, C., & Lambert, D. L. 1995, PASP, 107, 251
Valenti, J. A., & Fischer, D. A. 2005, ApJS, 159, 141
Vogt, S. S., Allen, S. L., Bigelow, B. C., et al. 1994, Proc. SPIE, 2198, 362
Walkowicz, L. M., & Basri, G. S. 2013, MNRAS, 436, 1883
Weiss, L. M., & Marcy, G. W. 2014, ApJL, 783, L6
Wizinowich, P. L., Le Mignant, D., Bouchez, A., et al. 2004, Proc. SPIE, 5490, 1
Wolfgang, A., & Lopez, E. 2015, ApJ, 806, 183
Wolfgang, A., Rogers, L. A., & Ford, E. B. 2016, ApJ, 825, 19
Yee, S. W., Petigura, E. A., & von Braun, K. 2017, ApJ, 836, 77